Scholars' Mine

Fall 2019

Small satellite earth-to-moon direct transfer trajectories using the CR3BP

Garrett Levi McMillan

SMALL SATELLITE EARTH-TO-MOON DIRECT TRANSFER TRAJECTORIES

USING THE CR3BP

by

GARRETT LEVI MCMILLAN

A THESIS

Presented to the Graduate Faculty of the

MISSOURI UNIVERSITY OF SCIENCE AND TECHNOLOGY

In Partial Fulfillment of the Requirements for the Degree

MASTER OF SCIENCE

in

AEROSPACE ENGINEERING

2019

Approved by:

Dr. Henry Pernicka, Advisor
Dr. David Riggins
Dr. Serhat Hosder

ABSTRACT

The CubeSat/small satellite field is one of the fastest growing means of space exploration, with applications continuing to expand for component development, communication, and scientific research. This thesis study focuses on establishing suitable small satellite Earth-to-Moon direct-transfer trajectories, providing a baseline understanding of their propulsive demands, determining currently available off-the-shelf propulsive technology capable of meeting these demands, as well as demonstrating the effectiveness of the Circular Restricted Three Body Problem (CR3BP) for preliminary mission design. Using the CR3BP and derived requirements from NASA's Cube Quest Challenge, five different trajectory scenarios were analyzed for their propulsive requirements. Results indicate that the CR3BP is an effective means for preliminary mission design; however, limitations were noted in its ability to account for the lunar orbit eccentricity with respect to the Earth. Additionally, two available options of off-the-shelf propulsion systems are identified that can achieve the ΔV necessary for lunar capture, but have not yet been demonstrated in-flight.

ACKNOWLEDGMENTS

TABLE OF CONTENTS

Page

SECTION

LIST OF ILLUSTRATIONS

LIST OF TABLES

1. INTRODUCTION

Traditional satellites are large, complex, expensive to build and launch, and often require government funding [1]. The CubeSat picosatellite platform aims to provide the opposite through a standard designed to minimize risk for the launch vehicle and increase launch opportunities for the CubeSat manufacturer [2, 3, 4]. Recently, advances in technology have enabled miniaturization of commercially available products, making CubeSats even easier and quicker to design and build, leading to a reduced timeline and launch opportunities within one to two years [1, 2, 4]. Furthermore, these advancements have resulted in increased interest from both private parties and government-funded projects, stimulating the industry through the launching of 471 satellites following the CubeSat standard as of August 2016, making CubeSats one of the fastest growing means of space exploration and research [1, 4].

1.1. CUBESAT STANDARD

California Polytechnic State University (Cal Poly) and Stanford's Space Systems Development Laboratory (SSDL) collaborated on a design called the "CubeSat standard" in 1999, and the first four CubeSats were launched into orbit on June 30, 2003 [2, 3, 5]. The CubeSat standard is a set of dimensions that define a small satellite for use within the Poly-Picosatellite Orbital Deployer (P-POD), and was originally designed as an educational tool and a low-cost means for technology demonstration [1, 2, 4]. This standard serves many benefits to companies, developers, and even students, providing improved accessibility to space, allowing pupils to participate in the full lifecycle of development, and additionally allowing for later launch procurement and last-minute swapping of payloads as a result of standardization [2, 3, 4].

CubeSats are not typically the primary payload on the launch vehicle and are often grouped together or with larger satellites; therefore, it is important to do no harm and limit the risk for nearby spacecraft or the launch vehicle. In order to accomplish this task CubeSats must first meet a set of general, mechanical, electrical, and operational requirements. Any deviation from these will necessitate a "Deviation Waiver Approval Request (DAR)" in order to integrate more fluid communication between all involved parties as well as aid in identifying potential concerns [2].

1.1.1. CubeSat Specifications. The specifications defined by the CubeSat standard provide specific rules and regulations regarding CubeSat deployment, operation, and size to reduce potential risk during integration and launch. It is necessary for the CubeSat to remain powered off and inactive until deployment [2]. Furthermore, a deployment switch on a rail standoff is required to mechanically disconnect all powered functionality of the spacecraft until after deployment [2, 3]. The CubeSat must also wait 30 minutes before activating deployables and 45 minutes before generation of any electro-magnetic signal [2]. All components must remain attached throughout launch, deployment, and operation so as to not increase space debris [2]. Moreover, CubeSats must also conform to NASA's procedural requirements (NPR 8715.6) and reenter the atmosphere with less than 15 joules of energy [2, 6]. Additionally, no pyrotechnics are permitted, the propulsion system requires a minimum of three inhibits to activate, total out-gassing mass loss should be below 10%, chemical energy prior to deployment should be below 100 watt-hours, and hazardous materials must follow the Air Force Space Command Manual (AFSPCMAN 91-710 Vol 3) [2, 7].

The standard shape of a CubeSat is a 10 cm cube, or a 1U, which can be combined to make larger volume satellites such as 2U, 3U, etc. [4, 8]. The main structure and rails of the CubeSat must be made of hard anodized aluminum such as 7075, 6061, 5005, and 5052 [2]. Each CubeSat is also permitted to have a mass up to 1.33 kg for each 1U of volume [2, 8]. The center of mass must be within 2.0 cm of the geometric center along the X and Y

axes of the CubeSat, where the Z axis is defined as parallel to the longest axis of the P-POD [2]. The center of mass restriction along the Z axis depends on the size of the CubeSat: 1U is required to be within 2.0 cm, 2U must be within 4.5 cm, and at or above 3U are required to be within 7.0 cm of the geometric center [2, 3].

1.1.2. Poly-Picosatellite Orbital Deployer. California Polytechnic State University is responsible for developing and maintaining the Poly-Picosatellite Orbital Deployer (P-POD) design, which offers protection for the CubeSat, launch vehicle, and other payloads [2]. Providing a standard interface for launch vehicles and constructed of anodized aluminum, the P-POD reduces risk and effort for the launch provider [2, 3]. Additionally, the inclusion of backwards compatibility in P-POD designs ensure that updates will not negatively impact missions in development [3]. In addition to protecting payloads, another function of the P-POD is to deploy the CubeSats. This is achieved via a deployment signal from the launch vehicle that initiates a sequence whereby a torsion spring opens the door, allowing the main spring to push CubeSats along the rails to exit [2, 3]. P-PODs are capable of holding up to three 1U CubeSats set apart by separation springs; however, CubeSats of different sizes can be arranged to share the space as well [2]. Furthermore, CubeSats with a volume of 3U and larger also have an extra space available within the P-POD to utilize known as the "Tuna Can," which is a cylindrical volume with a diameter less than or equal to 64 mm and a depth of 36 mm [2].

1.2. CUBESAT APPLICATIONS

While CubeSats were originally envisioned as an educational tool and for low-cost component development, their applications have expanded far beyond this and are now capable of scientific research, data collection, and communication.

1.2.1. Educational Platform. The nature of CubeSat design provides quick and inexpensive development that continues to foster opportunities to inspire and teach future engineers and space scientists. Commercially available off-the-shelf (COTS) components

are becoming increasingly accessible, allowing universities easy access to necessary materials [4]. This allows for quicker development and cheaper cost expenditure. The ability to quickly design and develop CubeSats in less than two years provides students with an opportunity to gain experience and make a real impact in the project, seeing it through from beginning to end [5]. As previously mentioned, the cost of constructing a CubeSat is relatively low (approximately $16,000) which allows institutions to more easily provide the necessary funds [9]. Furthermore, the cost from design to launch can range from $50,000 to $200,000 [8]. These factors alone enable educational institutions to implement CubeSat programs and coursework within the curriculum.

Furthermore, multiple agencies have offered assistance through programs or competitions for educational institutions working on CubeSat projects. The European Space Agency (ESA) offers the "Fly Your Satellite!" program that provides guidance on the project and access to testing facilities [10]. NASA's CubeSat Launch Initiative also aims to provide launches to space via ride-shares or deployment from the International Space Station [11]. Thus far, NASA has flown 58 CubeSats through this program, including those built by universities, tribal colleges, high schools, and even elementary schools, and has selected 149 more to be launched in the future [11].

Embedding CubeSat design, build, testing, and launching into a program offers a variety of benefits to students. In order to be successful, they must organize and develop teams and leaders, manage resources, schedule milestones, assign duties, and hold each other accountable for task completion, mirroring real-world work experience [8, 12]. CubeSat programs additionally require students of different disciplines to work together and communicate effectively, further promoting job field experience [8, 12]. The hands-on nature of building a satellite requires critical thinking to solve problems typically not offered in class as well as introducing students to a variety of interdisciplinary work.

1.2.2. Component Development. One of the primary benefits of CubeSats is the ability to purchase off-the-shelf hardware, including batteries, power management systems,

solar cells, propulsion systems, star trackers, reaction wheels, transmitters, antennas, etc. In the following paragraphs, some of the most commonly used components for spaceflight are discussed with regards to their availability and maturation.

1.2.2.1. Command and data handling. The ability of the communication hardware to transmit data from the CubeSat is the primary limiting factor for scientific research [1, 8]. Data storage, on the other hand, is readily accessible in high densities, allowing data to be stored and delivered over longer periods of time [1]. Because of this, further improvement in data storage is ineffective without simultaneous advancements in communication [1, 8]. Storage and transmission of the data are handled through a central computer that is available through multiple manufacturers, including Endurosat and Innovative Solutions in Space [13, 14]. Common processors utilized in the central computer include: Advanced RISC Machine (ARM) microcontrollers, Field-Programmable-Gate-Arrays (FPGA), MSP by Texas Instruments, and Peripheral Interface Controller (PIC) [1]. Arduino, BeagleBone, and Raspberry Pi are several open source hardware and software packages that have also been embraced by the CubeSat community [1]. Although the paramount benefit of these computers is their small size, one of their largest limitations is their limited resistance to radiation, and in order to fly deeper into space this obstacle will have to be overcome [1].

1.2.2.2. Communication. As mentioned in the previous paragraph, one of the current limitations of CubeSats is the ability to transmit large volumes of data [1]. Despite this, several manufacturers have succeeded in producing transmitters and antennas which are available off-the-shelf for very high frequency (VHF), ultra high frequency (UHF), and S-band frequencies; nevertheless, scientific research using CubeSats requires higher throughput than these technologies allow (1.2 kbps, 9.6 kbps, and 2 Mbps respectively), resulting in the inability to transmit data efficiently [1, 15, 16, 17, 18]. Although newer to the CubeSat market, X-band and Ka-band transmitters and antennas offer tens of Mbps; however, they continue to require some development before becoming mainstream [1, 17, 18]. The fastest communication technology being developed is optics/lasers which is

capable of exceeding 1 Gbps of data transmission and will enable more scientific research to be completed with CubeSats [1, 19]. Furthermore, the advancement of antennas through miniaturization and collapsibility may result in improved throughput, thus allowing for research farther into deep space.

1.2.2.3. Energy capture and storage. As CubeSats continue to expand beyond LEO, the requirements for energy storage, capture, management, and distribution become more demanding. Many of the products necessary to fulfill these needs are commercially available, including batteries, power management systems, and solar panels. Depending on the requirements of the specific satellite, two options for batteries are available – lithium-ion and lithium polymer [1]. Lithium polymer batteries are useful in unusually shaped volumes, but do not have as high an energy density as lithium-ion batteries [1, 20]. Additionally, lithium polymer batteries do not perform as well as lithium-ion in low temperature conditions, requiring a heat source for optimal performance [20]. Various power management systems manufactured by Blue Canyon Technologies, Clyde Space, and GomSpace are also available in order to recharge these batteries and deliver power to satellite components [1, 21]. Furthermore, power generation is an important aspect of most satellites and is typically accomplished via body-mounted or deployable solar arrays [1]. Triple junction solar cells for CubeSats are now achieving between 27 and 33% efficiency, allowing a 3U CubeSat with deployable solar cells to generate 20 to 30 W of power [1].

1.2.2.4. Guidance, navigation, and control. Guidance navigation and control (GNC) hardware has recently experienced significant improvement in miniaturization into a CubeSat format. The necessity for CubeSats to perform orbit determination on board and in space has prompted companies, such as Pumpkin, NanoAvionics, and SkyFox Labs, to make receivers that utilize a global navigation satellite system (GNSS) for the CubeSat form factor [22, 23, 24]. Global navigation satellite systems include Global Positioning System (GPS), Galileo, and Global Navigation Satellite System (GLONASS) [25, 26]. However, once a satellite travels farther into deep space, and these systems no longer function, radio

transponders become the primary mode of position and velocity determination [1]. Attitude determination hardware is usually paired with reaction wheels, magnetorquers, and/or thrusters to control the orientation of a CubeSat [1]. The most common means of attitude determination among all spacecraft is through the use of a star tracker; however, this technology remains newer in the realm of CubeSats, where star trackers are limited by sensor size and are now demonstrating arcsecond accuracy [1]. Star trackers are available from multiple vendors such as NanoAvionics, Blue Canyon Technologies, and Sinclair Technologies [1, 23, 27, 28]. Several manufactures, additionally, make an attitude control system that combines a star tracker and set of reaction wheels, such as the XACT and XACT-50 made by Blue Canyon Technologies [1, 29]. Other hardware utilized for attitude determination includes Sun sensors and magnetometers, but these are far less accurate than a star tracker [1].

1.2.2.5. Propulsion systems. Propulsion systems are vital in enabling satellites to change orbits, avoid collisions, and control entry into the atmosphere. Development in this area has grown recently with multiple manufacturers offering a variety of propulsion options. COTS manufacturers, such as ACCION Systems, Aerojet Rocketdyne, Busek Co. Inc., NanoAvionics, Tethers Unlimited Inc., and VACCO, produce systems capable of over 3700 newton-seconds of total impulse, thrust ranging from micronewtons to newtons, and specific impulse ranging from 40 seconds to 4000 seconds [1, 30].

Aerojet Rocketdyne is offering multiple propulsion systems designed for 3U and 6U CubeSats [31]. The MPS-120-2U is a 2U system capable of around 250 m/s of ΔV for an 8.0 kg satellite using only 1.0 kg of hydrazine [31]. The MPS-130-2U, however, uses 1.4 kg of green (AF-M315E) monopropellant and produces around 380 m/s of ΔV for an 8.0 kg spacecraft while in the same volume [31]. The BGT-X5 is made by Busek Co. Inc. with a 0.5 newton thruster and a specific impulse between 200 and 225 with the volume of 1U plus the tuna can [32]. Additionally, it is able to accelerate a 4.0 kg CubeSat by 146 m/s and the propellant tank volume can be increased for applications requiring more ΔV

[32]. It is noted that increasing the size of the propellant tank takes up more volume in the spacecraft. Busek also makes the BIT-3, an ion thruster capable of 2.5 km/s of ΔV for a 14.0 kg spacecraft using only 1.5 kg of its propellant, iodine [33]. The power requirement for this system, however, is 56-80 watts depending on the thrust desired [33]. VACCO also chose to use green monopropellant in its Lunar Flashlight Propulsion System that requires 3U of volume, but offers 237 meter/second of ΔV for a 14.0 kg satellite by using four 0.1 newton thrusters and 2.0 kg of propellant [34]. This equates to 478 m/s for a typical 8.0 kg 6U CubeSat [34].

Recently, CubeSats have launched with the following types of propulsion systems: chemical, cold gas, electrospray, pulsed plasma, resistojet, and vacuum arc [1]. Other CubeSats have even launched with propellantless systems such as a solar sail [1]. Currently, propulsion systems classified as a finite-burn comprise the majority of those utilized on CubeSats [35]. Although continuous-burn systems have also flown, these are less popular due to energy demands they place on the small spacecraft [35]. One such example is the CubeSat MEMS system manufactured by NanoSpace by GomSpace and flew on the TW-1 CubeSat [35]. This system produced a specific impulse between 60 and 92 seconds from heated butane [35]. Another example includes the Micro CubeSat Propulsion System made by VACCO for the JPL MarCO CubeSats [36]. It utilized R236fa propellant to produce 755 newton-seconds of total impulse with four thrusters at 0.25 newtons [36]. Several other cold gas systems that have flown are shown in Table 1.1. Using the Tsiolkovsky rocket equation in equation 1.1, the amount of ΔV can be estimated for a given specific impulse, total mass, and propellant mass. The max estimated specific impulse achieved from a mission with a cold gas system was 69 seconds and using 3.0 kg of fuel in an 8.0 kg spacecraft results in ΔV of 318 m/s.

$$\Delta V = I_{sp}g \ln \frac{M_i}{M_f} \qquad (1.1)$$

Table 1.1. Recently flown CubeSat propulsion systems [35].

Flown Propulsion Systems	Type	I_{sp} [s]
NANOPS	Cold Gas	46
CNAPS	Cold Gas	45
MEMS	Cold Gas	30
Micro-propulsion	Cold Gas	32
T^3-μPS	Cold Gas	69
U. of Texas custom	Cold Gas	64
CubeSat MEMS system	Electrothermal	60-92

1.2.2.6. Thermal. Like all satellites, CubeSats are exposed to the unusual thermal environment of space. In space, direct sunlight, albedo, infrared radiation from the Earth or Moon, and internal components all contribute to the thermal activity on-board [1]. A few means of passive thermal control include heat pipes, louvers, multi-layer insulation (MLI), Sun shields, radiators, thermal coatings, and thermal straps, which are all available off-the-shelf for CubeSats [1, 37, 38]. For biological experiments or infrared imaging, it is necessary to actively control temperatures through the use of heaters or cyrogenic cooling [1]. Cryogenic cooling technology requires maturation before becoming available off-the-shelf for CubeSats [1]. Additionally, as aforementioned, lithium polymer batteries are susceptible to cold temperatures, making thermal regulation a requirement not only for scientific research but for power as well [20].

1.2.3. Scientific Research. As the popularity and feasibility of CubeSats grow, so does the desire to implement their use as an affordable means of scientific research. Current areas of research encompass the Earth, deep space, and *in situ* experimentation. The following paragraphs focus on the current use of CubeSats as a method of scientific research, their limitations, and need for future expansion.

1.2.3.1. Earth research. A primary sensor that many satellites utilize in order to research the Earth's atmosphere and its components are radiometers. Because the miniaturization of radiometers is new, this technology requires further testing in order to fully incorporate its use in CubeSats. Although the use of CubeSats to address the research of

Earth's surface properties has not been fully demonstrated in-flight, the use of radiometers in measuring these data is well documented among traditionally-sized satellites. Radiometers have become vital tools in studying aerosols and cloud characteristics [1, 8]. Many features of the Earth's surface can also be assessed with the use of radiometers. Traditionally, radiometers have measured radiance to capture information regarding soil moisture, ocean surface wind speed, temperature, and salinity, ice sheet topography, and snow cover [1, 8]. Furthermore, larger satellites have also used these tools to research vegetation in terms of the Normalized Differential Vegetation Index (NDVI) and Photochemical Reflectance Index (PRI) [8]. In addition to capturing atmospheric properties, radiometers can also measure the intensity of radiation expelled and reflected from Earth [1, 8]. Moreover, when including cooled and uncooled microbolometers, radiometers are able to measure Earth's surface temperature [8].

CubeSat projects, such as IceCube and MicroMAS-2, have demonstrated the feasibility of implementing radiometers in-flight to assess aerosols [1, 8, 39, 40]. MicroMAS-2 used a radiometer to capture data regarding atmospheric temperature and moisture [1, 8, 39]. IceCube, a 3U satellite, on the other hand, demonstrated the benefits of implementing radiometers in order to assess cloud properties, such as particle size and ice mass [1, 40]. CubeSats have also been successfully launched to demonstrate the functionality of a CubeSat to capture data regarding radiation budget with a radiometer [1, 8]. For example, RAVAN, a 3U CubeSat launched in 2016, not only measured radiance and demonstrated a CubeSat's ability to monitor the Earth's radiation budget, but further displayed the potential for a global constellation [1, 41]. MiRaTA also carried a radiometer to assess atmospheric temperature profiles, moisture profiles, and cloud ice [42].

With CubeSat technology continuously expanding, many future launches have been planned. Future CubeSats carrying radiometers will capture data regarding tropospheric temperature as in PolarCube [1, 43]. Several other CubeSats that will implement radiometers worth noting are TEMPEST-D, PICASSO, and CIRiS [1]. TEMPEST-D, a 6U CubeSat will

collect data regarding the formation and dispansion of clouds, while PICASSO, 3U, will access stratospheric ozone and atmospheric temperature profiles [1, 44, 45]. Finally, CIRiS, which is a 6U CubeSat with an uncooled microbolometer, will capture data regarding water and land management [1, 46].

In addition to radiometers, spectrometers can gather valuable information on Earth and its atmosphere. Not only can spectrometers capture data regarding characteristics of aerosols, snow cover, atmospheric temperature, precipitation and humidity, cloud properties, vegetation mapping, and land use, but they are also able to gather information regarding algae mapping, wildfire monitoring, and greenhouse gas composition and density [1, 8]. When incorporated on a CubeSat, spectrometers assist in gathering information on the makeup and density of greenhouse gases in Earth's atmosphere, including CH_4, CO, CO_2, HF, H_2O, O, and O_3 via total column measurements [8]. CubeSats demonstrating the ability of this technology to capture data regarding greenhouse gases, such as CanX-2, a 3U CubeSat with a 1 km horizontal resolution, and SathyabamaSat, a 2U CubeSat, have already been launched [1, 47, 48]. Furthermore, the spectrometer housed on CanX-2 has spectral and spatial resolutions also capable of capturing NDVI information; however, this is not currently its primary function [8]. Additionally, Aalto-1 uses a spectrometer to gather data regarding cloud properties, wildfire monitoring, vegetation, and algae mapping [8, 49]. Other CubeSats, such as MicroMAS-2 used a radiometer in conjunction with a spectrometer to gain further knowledge about the Earth's atmosphere, of which the spectrometer portion is responsible for assessing temperature, precipitation, and humidity [1, 8, 39]. Finally, CIRAS, a 6U CubeSat planned for a launch in 2019, will be responsible for collecting temperature and water vapor measurements using a spectrometer cooled by a cryocooler [1, 50, 51].

GNSS occultation and reflectometry are newer assets that further provide additional means of collecting data regarding Earth and its atmosphere [1]. Reflectometry has the potential to provide information on vegetation, ocean and ice altimetry, and ocean salinity;

however, until recently this technology has been too been too large for CubeSat integration [8]. Furthermore, GNSS reflectometry could be further used to perform scatterometry to provide information regarding soil moisture, biomass, and wind speed and direction [1]. The 6U [3]CAT-2 is a forerunner in implementing GNSS reflectometry among CubeSats, and has demonstrated the ability to scale-down and incorporate a receiver [1, 52]. The main function of [3]CAT-2 is to collect data on ocean altimetry [52]. GNSS occultation, however, is easier to implement and can be found on CubeSats such as GOSTE, ARMADILLO, EON-MW, MiRaTA, and CanX-2, and allows for the observation of atmospheric temperature, pressure, density, and humidity, as well as ionospheric electron content and density profiles [1]. CanX-2, mentioned in the previous paragraphs, also houses GNSS occultation technology that is capable of observing the total electron content in the ionosphere and trophospheric H_2O vapor [47]. MiRaTA houses a GNSS occultation receiver, in addition to its radiometer, that is responsible for assessing upper neutral atmospheric temperature and pressure profiles as well as ionospheric electron density [42].

Although radiometers, spectrometers, and GNSS receivers have a wide variety of uses among all varieties of satellites, alternative methods for capturing data regarding Earth and atmospheric research are also available for use with CubeSats. Gamma ray detectors, photodiodes, and VLF receivers have been used in combination to study lightning and terrestrial gamma ray flashes (TGF), and were demonstrated in-flight by Firefly in 2013 and will be further exhibited by TRYAD-1 and 2, once launched [1, 8, 53]. Additionally, polarimeters are used for measuring aerosol size, shape, and composition, and were also demonstrated on the 3U CubeSat HARP, which focused on the droplet size and distribution width of particles within clouds [1, 54]. Other CubeSat technologies include Langmuir probes, electric field probes, and magnetometers, which have all been demonstrated by DICE in 2011, during its research on plasma density as well as AC and DC electric and magnetic fields [1, 55]. Collecting these data will enable DICE to investigate the formation of Storm Enhanced Density bulge within the ionosphere [1, 55]. In 2012, CINEMA was

launched into a low Earth orbit with two scientific instruments: Suprathermal, Electrons, Ions, and Neutrals particle detector and two magnetoresistive magnetometers placed inboard and on a deployable one-meter stacer boom, allowing observation of Earth's ring current, particle precipitation, and magnetic field [1, 56].

As noted multiple times in the aforementioned paragraphs and sections, CubeSat technology is ever-changing and developing, and because this technology is newer, other sensors that are widely-available to traditionally-sized satellites are currently not compatible with the power and size constraints of CubeSats. Lidars and radars, for example, can use a real or synthetic aperture to capture data regarding land, vegetation, and ice sheet structure or topography; however, more research and development will be necessary in these areas before this becomes a beneficial option in Earth research using CubeSats [8]. In addition to these areas of inquiry, radars have further demonstrated the ability to gather data regarding snow cover and ocean altimetry, and although the use of radar to assess sea ice cover has not yet been demonstrated, this has previously been explored as well [8]. Even though power and size requirements significantly limit the use of radar in CubeSats, RainCube, a 6U CubeSat, has demonstrated the ability to implement a radar on-board to collect information on precipitation and snowfall; however, this is possible secondary to a deployable antenna, which effectively lowers the energy demand placed on the CubeSat by improving its efficiency in capturing the radar signal [8, 57]. Radar technology, like that of lidars, will have to be explored further to fully understand its power requirements in terms of CubeSats, specifically improving the ability to capture data (i.e antennas), as well as lengthening its available operational run-time. Finally, scatterometers are able to infer wind speed through analysis of ocean surface; however, are also limited by power requirements on-board [8].

1.2.3.2. Deep space. While the primary focus of CubeSats has been towards Earth, there is growing interest in using this platform for deep space exploration or researching other celestial bodies. The future of lunar research encompasses implementing CubeSats

for various experiments ranging from finding water, to near-surface hydrogen, and even to the study of the polar regions [1]. Several CubeSats are currently destined for lunar research within the coming year [1]. Lunar IceCube is one of these and will carry the Broadband Infrared Compact High Resolution Explorer Spectrometer (BIRCHES) to look for water in various states, as well as other volatiles [1, 58]. The 1,000,000 pixel detector is responsible for capturing infrared signals and determining the different phases of water [1, 58]. While other full-size satellites have performed similar tasks with regards to lunar water, none were as effective as BIRCHES for this task [58]. LunaH-Map, a 6U CubeSat carrying two neutron spectrometers capable of counting neutrons within the top one meter of the lunar surface at a 7.5 km per pixel resolution, will also be mapping water deposits on the Moon [1, 59]. Lunar Flashlight is another 6U CubeSat that will map out ice around the lunar polar regions using near infrared lasers to illuminate shaded regions and a spectrometer to measure the surface reflection and composition [1, 60, 61].

NEAScout will travel beyond the Moon and is planned to encounter 1991VG, a near-Earth asteroid [1]. Maneuvering will be accomplished via an 86 m^2 solar sail and a cold-gas propulsion system [1, 62]. This will enable the multispectral camera to capture images for navigation as well as research to estimate properties like shape, pole position, spin rate, and regolith properties of 1991VG [1, 62]. MarCO is a set of two identical 6U CubeSats that performed a Martian flyby in November of 2018 and relayed data between InSight and the Deep Space Network (DSN) [1]. Communication with Insight was accomplished using UHF and X-band for DSN [1]. Potentially even farther from Earth will be INSPIRE, a set of two identical 3U CubeSats being sent on an Earth-escape trajectory for deep space. Each satellite contains a vector-helium magnetometer to measure solar wind [1, 63, 64]. The launch of NASA's SLS will put CuSP into deep space as well to characterize low-energy solar energetic particles using the Suprathermal Ion Spectrograph, count high-energy solar energy particle with the Miniaturized Electron and Proton Telescope, and the Vector Helium Magnetometer will measure strength and direction of magnetic fields of the Sun [1, 65].

Several CubeSat projects have even set their goals on objects beyond our solar system. Utilizing a cadmium zinc telluride detector, the CXBN 2U CubeSat takes measurements of the Cosmic X-Ray Background in the 30-50 keV range to map the Extragalactic Diffuse X-Ray Background [1, 66]. ASTERIA is a 6U CubeSat that was launched in 2017 with the purpose of searching for transits of identified radial velocity planets [67, 68]. These are planets that have been discovered using the radial velocity technique whereby a star moves in a radial direction with respect to the observer due to the gravitational pull of a nearby planet causing a doppler effect on the star's light [1, 67, 68, 69]. ASTERIA captures transits by performing high-cadence, long-duration stellar photometry using a CMOS imager [1, 67]. PicSat, a 3U CubeSat, will also be performing photometry, but its primary mission is only for the transit of Beta Pictoris b [1, 70]. PicSat has a photometer with a 3.5 cm telescope to monitor the transit and determine Beta Pictoris b's radius, Hill sphere, and characterize the debris disk [1, 70]. Another 6U CubeSat, HaloSat, was deployed from the International Space Station (ISS) and contained three off-the-shelf X-ray detectors to map the Milky Way's oxygen line emission [71]. These data will help answer the question of whether there is a hot gaseous cloud of oxygen around the Milky Way and help resolve the astrophysics problem of the missing baryon [1, 72].

1.2.3.3. *In Situ*. Another interesting area where CubeSats are being used for research is *in situ* experiments. One of the first CubeSats to contain a biological experiment was Pharmasat, a 3U CubeSat that contained yeast cells that were provided three different doses of an antifungal agent to analyze their response and the effectiveness of the treatments in a space environment [1, 73]. Instead of fungus, O/OREOS hosted a bacterial experiment as well as an organic compounds experiment [1, 74]. The bacterial experiment used two different bacteria and included rehydrating, feeding, and growing them to test their response in microgravity and radiation [74]. The organic molecules were exposed to radiation and microgravity as well to assess the stability of the compounds [1, 74]. SporeSat's experiment involved testing plant cell growth from spores in microgravity [75]. This experiment also

includes testing the application of artificial gravity through rotating the CubeSat [75]. The first CubeSat with a biological experiment to travel beyond low Earth orbit will be BioSentinel [1]. Biosentinel is a 6U CubeSat manifested on EM-1 of NASA's SLS [1, 76]. Its experiment will investigate the effects of deep space on DNA within genetically modified yeast cells. [1, 76]. Q-PACE and AOSAT missions are focused on the interaction between materials and objections in space. Q-PACE is a 2U CubeSat investigating protoplanetary disk and ring formations by recording collisions between four different particle samples at speeds from 1 mm/s to 10 cm/s [77]. AOSAT is 3U and will act as a centrifuge and rotate up to 4 rpm around its minor axis in order to provide similar acceleration as the gravity on a 1 km asteroid [78]. The two outer 1U volumes will contain crushed meteorites and dust for the experiment to investigate surface properties of asteroids [1, 78].

1.3. LUNAR LAUNCH OPPORTUNITIES

Currently, there are multiple launch opportunities available for CubeSats, each with varying degrees of performance. Many companies are capable of launching CubeSats into low Earth orbit (LEO); however, in the context of this study, the main focus of CubeSat launch opportunities is placed on those capable of trans-lunar injection (TLI). Additionally, to maintain within the scope of this research study, NASA's Space Launch System and Exploration Mission-1 is discussed at a greater length in order to provide understanding and context.

Northrop Grumman Innovation Systems, formerly Orbital ATK, has a long-standing history of launching CubeSats on their Minotaur series of rockets. Although Minotaur Commercial and Minotaur I are not capable of TLI, each vehicle has demonstrated the ability to effectively launch CubeSats, including, the SkySat mission and Orbital Responsive Space-3 (ORS-3) mission [3, 79, 80]. Minotaur V, though has not demonstrated the ability

to launch a CubeSat, is capable of TLI of a payload up to 447 kg [81]. Also developed by Northrop Grumman is Antares, which has launched CubeSats into LEO and can perform TLI of a payload up to 232 kg [79, 82].

Rocket Lab has recently demonstrated the capability of their rocket, Electron, to launch small satellites into LEO and is unique in that it was designed specifically for launching CubeSats and other small satellites [43, 83]. Electron is capable of TLI injection with 10 kg of payload and will demonstrate this for the upcoming Moon Express mission [82, 84]. Another launch provider primarily focusing on small satellites is Virgin Galactic, who is planning to launch LauncherOne within the coming year [43, 85].

Another company that has previously launched CubeSats is SpaceX [79]. SpaceX's Falcon 9 rocket launched multiple CubeSats during the SpaceX-3 and SpaceX-12 missions, and is capable of sending 653 kg of payload to the Moon [79, 82]. Furthermore, another SpaceX launch vehicle, Falcon Heavy, recently demonstrated the performance to launch a payload beyond the Earth-Moon system, and has launched CubeSats on the Space Test Program (STP)-2 mission [43].

United Launch Alliance (ULA) has launched CubeSats on two of its launch vehicles, Delta II and Atlas V [79]. Delta II has successfully accomplished three missions carrying CubeSats for NASA's Educational Launch of Nanosatellites (ELaNa) and has one more planned within the year [43, 79]. Furthermore, Delta II is capable of sending CubeSats to the Moon as it can carry up to 1250 kg on an Earth-escape trajectory [86]. Additionally, Atlas V has flown six total missions with ELaNa ride-shares and is further capable of carrying up to 1110 kg to the Moon [79, 82].

Finally, some of the first launch vehicles to carry CubeSats were the Rockot, made by Eurockot Launch Services, and DNEPR, made by International Space Company (ISC) Kosmotras [3]. While these vehicles are not capable of directly sending payloads to the Moon, when provided supplemental propulsion systems they are able to achieve a TLI [87, 88].

1.3.1. Space Launch System. A forerunner in supporting the CubeSat initiative is NASA, which, as mentioned above, provides ride-share opportunities for CubeSats developed by educational institutions [11]. While NASA does not currently have a launch vehicle on which to place CubeSats, it is currently developing the Space Launch System. The SLS is an exploration-class launch vehicle managed at the Marshall Space Flight Center (MSFC) to propel astronauts and cargo beyond Earth orbit (BEO) to potential destinations such as Lagrange points, asteroids, the Moon, and Mars [89, 90].

1.3.2. Exploration Mission-1. The SLS's first flight will be Exploration Mission-1 (EM-1) to test systems for the SLS and Orion in 2020 [91, 92]. This is an un-crewed flight with an initial fly-by free-return trajectory of the Moon and an approximate duration of 26 days [89, 91, 93, 94]. After launch from Cape Canaveral at Launch Complex 39B, the core stage will inject the interim cryogenic propulsion stage (ICPS) and Orion in an elliptical LEO where the ICPS will perform two burns: the first to raise perigee to a 185 x 1806 km orbit and the second for TLI. This is followed by separation of Orion and the ICPS; [91, 94]. Orion will perform a series of burns to fly ahead of the Moon's path and enter a Distant Retrograde Orbit (DRO) at a distance of 70,000 km using the European Space Agency's (ESA) supplied Service Module [91, 94]. Elapsed time in the DRO will range between six and nine days before another series of burns is completed, putting Orion on a return trajectory back to Earth with an atmospheric entry speed near 11 km/s [89].

Although the ICPS will have separated from Orion, its mission is not yet complete. Once Orion is safely out of range, the ICPS will deploy 13 CubeSats. Each CubeSat is 6U and initially on a fly-by trajectory behind the Moon, headed to deep space. Several satellites including Lockheed Martin's Skyfire, NASA's Near-Earth Asteroid Scout (NEA Scout), NASA's BioSentinel, and NASA's CubeSat for Solar Particles (CuSP) will continue on this trajectory to perform their given missions [62, 65, 95]. Lunar Flashlight, Morehead

State University's Lunar IceCube, Arizona State University's Lunar Polar Hydrogen Mapper (LunaH-Map) and others will perform orbital maneuvers to inject into orbit about the Moon to accomplish their mission [58, 59, 60].

1.4. LITERATURE SURVEY

The purpose of this section is to show the relevant history of human and robotic spaceflight lunar missions. These missions were manned and unmanned and utilized different types of transfers. It is worth noting how many of these missions were direct transfers compared to low-energy and low-thrust.

1.4.1. Lunar Missions. The launch of Sputnik occurred on October 4, 1957. Less than a year afterward, humans were attempting to send a spacecraft to the Moon [96]. The first attempt by any country was an Able 1 satellite launched on a Thor-Able 1 launch vehicle on August 17, 1958 by the United States [97]. This was the first of seven between the United States of America (US) and the Union of Soviet Socialist Republic (USSR), four and three respectively, to fail at reaching the Moon [97]. The eighth attempt was by the USSR on January 2, 1959 aboard an 8K72 launch vehicle [97]. The retroactively named Luna 1 satellite reached a lunar altitude of 6,400 km 34 hours after launch and continued into deep space to become the first human spacecraft to orbit the Sun [97].

The first successful launch to impact the Moon occurred on September 12, 1959 by the USSR [97]. This was the eleventh mission overall and sixth for USSR targeting the Moon. The next flight by the USSR was also successful with the first photographs taken of the far side of the Moon (Figure 1.1). These two satellites were retroactively known as Luna 2 and Luna 3, respectively [97].

On January 31, 1966, the USSR launched Luna 9, which landed on the Moon and sent the first image to Earth from the surface of any celestial body [97]. This was quickly followed by the launch of Luna 10 on March 31, 1966 and two days later became the first human-made object to orbit the Moon with a prograde, 79.1° inclination, 350 x 1,000 km
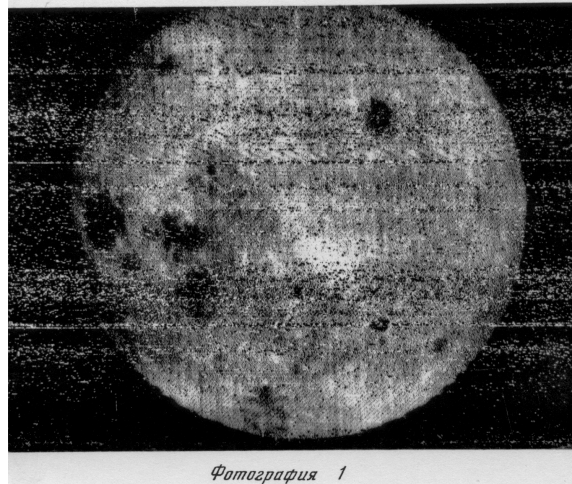
Figure 1.1. This is the first image of the far side of the Moon taken by Luna 3, October 3 1959, 3:30 UT [97, 98].

orbit [97]. The first true soft-landing on the Moon was by Surveyor 1 launched by the U.S. on May 30, 1966; Surveyor 1 also sent back 11,350 pictures [97]. The U.S. became the second nation to orbit the Moon using Lunar Orbiter 1 on August 24, 1966 with a prograde, 191 x 1,854 km orbit [97]. Its primary objective was to photograph potential Apollo landing sites, secondary landing sites, and Surveyor 1; although, its most famous photograph is the first Earthrise image taken from the Moon [97]. This was followed by Lunar Orbiter 2, 3, 4, and 5 which successfully achieved orbits of 196 x 1,871 km, 200 x 1,850 km, 200 x 1,850 km, 2,705 x 6,034 km, and 196 x 6,040 km respectively [97].

The first circumlunar flight occurred in September 1968 with Zond 5 passing ahead of the Moon at an altitude of 1,950 km before returning to Earth [99]. The USSR satellite carried several biological payloads including two steppe tortoises, wine flies, meal worms, plants, seeds, bacteria, and others [97, 99]. These payloads safely splashed down in the Indian Ocean following a ballistic unguided reentry due to two failed attitude control sensors [97, 99].

Three months later, on December 21, the US "followed suit" but this time the "biological payload" was three humans, Borman, Lovell, and Anders [100]. The mission

included a 66.3 hour transfer duration along a free-return trajectory ahead of the Moon followed by a 915 m/s ΔV to achieve lunar orbit insertion [96, 100]. The low lunar orbit was circularized from 111 x 312 km to a 112 km altitude orbit [100]. After 20.27 hours in lunar the orbit, the trans-Earth injection maneuver was initiated and initiated the trip back to Earth [101]. The mission concluded with a successful splashdown in the Pacific Ocean.

Figure 1.2. Famous Earthrise photo taken by Michael Anders as Apollo 8 emerged from behind the Moon [102].

Just over six months later the US launched towards the Moon for another first, lunar landing. Apollo 11 launched July 16, 1969 with three humans on board, Collins, Aldrin, and Armstrong [100]. Translunar injection occurred with a velocity of 35,545.6 ft/s [101]. Like Apollo 8, it was a free-return trajectory and with a slightly longer duration of 73 hours 5 minutes and 34.83 seconds. The Command/Service Module (CSM) and docked Lunar Module (LM) entered a lunar orbit of 169.7 x 60.0 nautical miles and then was lowered to 66.1 x 54.5 nautical miles. The LM undocked with Aldrin and Armstrong inside and inserted into a 58.5 x 7.8 nautical mile orbit before a 753.39 seconds-long powered descent and landing. After 21 hours 36 minutes and 20.9 seconds of activity on the lunar surface the LM launched from foreign soil to 48.0 x 9.4 nautical mile orbit. Several stage burns and

orbits were necessary to rendezvous and dock with the CSM after being undocked for 27 hours and 51 minutes. Following crew and cargo transfer to CSM, the LM was undocked to remain in decaying lunar orbit until crashing [100]. At a velocity of 8,589.0 ft/sec the CSM entered a trans-Earth orbit that lasted of 59 hours 36 minutes 52 seconds. Due to poor weather, landing was moved 215 nautical miles downrange and involved a successful recovery.

Subsequent Apollo missions were initially placed on a free-return trajectory, however around halfway a midcourse correction was performed to place the CSM/LM on a non-free-return circumlunar trajectory [101]. This enabled greater flexibility for launch. If the spacecraft was not capable of lunar orbit insertion, it was still possible to perform a maneuver and place it in a free-return trajectory to Earth. This is precisely what occurred for Apollo 13, which used the descent engine to place the modules back into a free-return trajectory.

Thus far all missions to the Moon were through a direct transfer and this would continue until the follow-on mission of Hiten, a Japanese spacecraft, which, on March 30, 1990, used a lunar flyby to increase apogee to 1,532,000 km [103]. This was the first utilization of a low-energy transfer to the Moon and first lunar capture without a ΔV; this was used as a technology demonstration for a future spacecraft, Geotail [103]. A similar case occurred for two satellites in 1991 during the THEMIS mission. After completing the full mission, the two outer satellites of the original five were given a mission extension to explore the Moon. These two were originally located in a highly elliptical Earth orbit and after over 40 maneuvers were placed on a low-energy transfer taking several months to enter lunar capture [104, 105, 106].

SMART-1 was launched on September 27, 2003 into a geostationary transfer orbit of 7,029 x 42,263 km [107]. The spacecraft then passed through multiple mission phases using its Hall effect thruster. The first mode included raising perigee to spiral outward and move outside of the Van Allen Belts, which can reach out 36,000 miles above the Earth's

surface, by continuously thrusting [96, 107, 108]. The second phase used thrusting only around perigee to move apogee closer to the Moon. The spacecraft was captured using lunar resonances just over a year later [107]. This is the only spacecraft to have used a low-thrust transfer to obtain lunar capture.

1.4.2. Lunar Trajectories. There are three main types of trajectories for transferring to the Moon: direct, low-energy, and low-thrust. Each has been used successfully to place a satellite in lunar orbit.

1.4.2.1. Direct transfers. Direct transfers are by far the most common type of transfer with around 100 missions to date and are sometimes referred to as the "conventional method" [96]. They are characterized by a short transfer duration between Earth and Moon at three to six days with the most fuel-efficient being around four and a half. Gravitational forces from the Earth and Moon system are the driving factors behind the trajectory design while other influences are treated as perturbations. The restricted three-body problem or patched-conic method are often used for designing a direct transfer. An additional benefit is that only one pass through the Van Allen Belts is necessary; although, Clementine and Chandrayaan-1 negated this benefit by using staging orbits to expand the launch period. Some notable direct transfer missions include Luna 1-24, Ranger 3-9, Zond 3 and 5-8, Surveyor 1-7, Lunar Orbiter 1-5, Apollo 8 and 10-17, International Cometary Explorer (ICE) (also known as International Sun-Earth Explorer-3 (ISEE-3)), and Lunar Prospector [96, 97].

1.4.2.2. Low-Energy transfers. Low-energy transfers are trajectories that employ the Sun's gravity to increase perigee to a lunar distance by extending the transfer far beyond the Moon for several months [96]. The spacecraft will then approach the Moon at periapsis with respect to the Earth (perigee); possibly with a negative orbital energy with respect to the Moon, lowering the ΔV necessary for lunar orbit insertion. Although the propulsive requirement for the spacecraft has been lowered, some has been shifted to the launch vehicle for placing the spacecraft at an apogee of 1-2 million km following a lunar flyby.

The transfer duration lasts between three and four months unless more lunar flybys are necessary with only one pass through the Van Allen Belts. A further benefit is a widened launch period compared to a direct transfer. Only 5% of successful lunar missions have utilized a low-energy transfer.

The first spacecraft designed and launched with a low-energy transfer was Gravity Recovery and Interior Laboratory (GRAIL) that included two satellites [96]. GRAIL had a launch period of 26 days and a transfer duration between 90 and 114 days. The two satellites were separated by 25 hours upon lunar arrival. To date there have been a total of five spacecraft to fly a low-energy transfer: Hiten, ARTEMIS P1, ARTEMIS P2, and the two GRAIL satellites [96, 104, 105].

1.4.2.3. Low-Thrust transfers. Utilizing a low-thrust transfer requires a propulsion system capable of thrusting for long periods of time, such as a solar electric propulsion system [96]. A characteristic of these transfers is a spiral shape as thrust continues to be applied in the orbital plane and perpendicular to the position vector. This also necessitates multiple passes through the Van Allen Belts. The SMART-1 satellite is the only example of a low-thrust transfer to the Moon with a total Earth-to-Moon duration of over a year.

1.5. THESIS STUDY OBJECTIVE

The purpose of this research study is to investigate Earth-to-Moon direct transfer trajectories focusing on those suitable for small satellites, 6U and under, and determine their viability given currently-available micropropulsion systems. Section 2 supplies a framework of understanding and a derivation of the dynamic models discussed throughout this thesis, including the circular restricted three-body problem (CR3BP) and coordinate conversions to and from the rotating and inertial frames. Section 3 details the initial definitions and parameters pertinent to small satellites that are utilized to investigate the study objective. Sections 4 and 5 review viable lunar trajectories for CubeSats and discuss their ability for future contribution to the aerospace community. A high-fidelity model is used to simulate

the resulting trajectories and demonstrate the effectiveness for preliminary mission design. This will enable projects with a similar mission concept to quickly and effectively establish design criteria as well as iterate on a working trajectory design.

2. DYNAMIC MODELS

This section includes a brief review of the restricted three-body problem and transforming coordinates from the Earth-centered inertial frame to the barycentric synodic coordinate frame of the restricted three-body problem.

2.1. RESTRICTED THREE-BODY PROBLEM

A synodic frame is defined with the origin located at the barycenter of two primary bodies (Earth and Moon in this study) of finite mass with the $\hat{x}$-axis pointing toward the smaller, the $\hat{z}$-axis parallel to the specific angular momentum vector, and the $\hat{y}$-axis completing the right handed system. This frame, therefore, rotates according to the orbital motion of the minor primary body around the major one with respect to the barycenter fixed frame as shown in Figure 2.1 and discussed in [109].
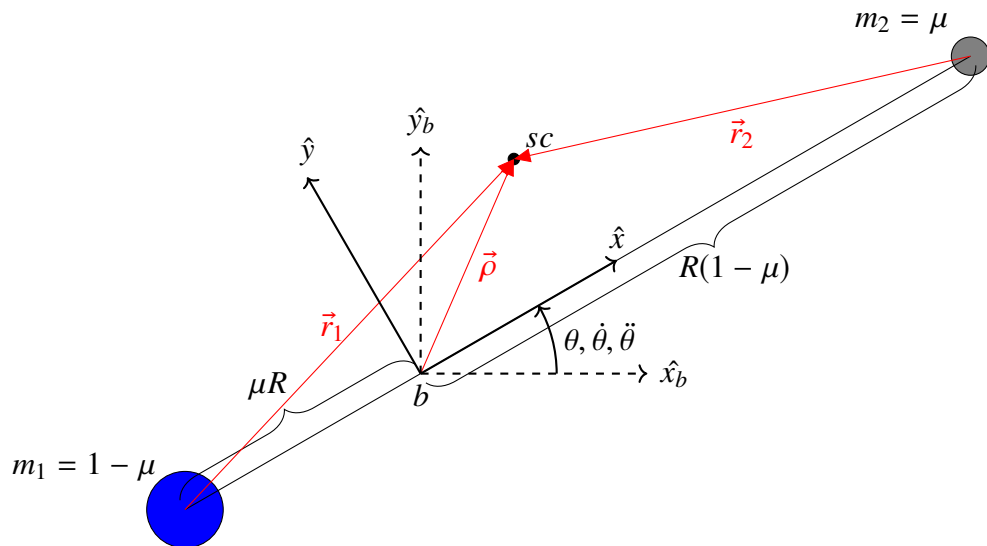
Figure 2.1. The barycenter inertial and synodic coordinate frames associated with the Restricted Three-Body Problem. The synodic frame ($\hat{x}$, $\hat{y}$, $\hat{z}$) rotates according to θ, $\dot{\theta}$, and $\ddot{\theta}$ with respect to the barycentric inertial frame ($\hat{x}_b$, $\hat{y}_b$, $\hat{z}_b$).

The equations of motion are expreseed using nondimensional units for length, mass, and time. The unitless mass dimension is equivalent to the sum of the two primary bodies, the length unit is defined as the distance between them (R), and the time unit is defined such that the gravitational constant is unity. The nondimensional mass of the second primary (μ) is also the nondimensional distance from the barycenter to the first primary; 1 - μ is used for the converse, as is discussed in [110].

The differential equations of motion for the elliptic restricted three-body problem (ER3BP) are then given by

$$\ddot{x} - 2\dot{\theta}\dot{y} - \ddot{\theta}y - \dot{\theta}^2 x = -\frac{(1-\mu)(x+\mu R)}{r_1^3} - \frac{\mu(x-(1-\mu)R)}{r_2^3} \tag{2.1}$$

$$\ddot{y} + 2\dot{\theta}\dot{x} + \ddot{\theta}x - \dot{\theta}^2 y = -\frac{(1-\mu)y}{r_1^3} - \frac{\mu y}{r_2^3} \tag{2.2}$$

$$\ddot{z} = -\frac{(1-\mu)z}{r_1^3} - \frac{\mu z}{r_2^3} \tag{2.3}$$

where

$$r_1 = \sqrt{(x+\mu R)^2 + y^2 + z^2} \tag{2.4}$$

$$r_2 = \sqrt{(x-R+\mu R)^2 + y^2 + z^2} \tag{2.5}$$

If the motion of both primaries around the barycenter is assumed to be circular, then angular velocity ($\dot{\theta}$) is constant and in nondimensional units becomes one. Angular acceleration ($\ddot{\theta}$) is, therefore, zero. This is then known as the "circular restricted three-body problem (CR3BP)."

Within the circular restricted three-body problem, Jacobi's Integral is the only integral of motion. It can be found by multiplying equations 2.1, 2.2, and 2.3 by their respective velocity and adding them together to form equation 2.6.

$$\ddot{x}\dot{x} + \ddot{y}\dot{y} + \ddot{z}\dot{z} - x\dot{x} - y\dot{y} - z\dot{z} = -\frac{(1-\mu)}{r_1^3}(\dot{x}(x+\mu R) + y\dot{y} + z\dot{z})$$
$$-\frac{\mu}{r_2^3}(\dot{x}(x-(1-\mu)R) + y\dot{y} + z\dot{z}) \tag{2.6}$$

Integrating equation 2.6 results in equation 2.7 where C is referred to as Jacobi's constant and is constant throughout the object's path. Jacobi's constant will only change when a force from outside the system, such as another perturbing body or spacecraft thrust, is applied to the spacecraft.

$$C = \frac{-1}{2}(\dot{x}^2 + \dot{y}^2 + \dot{z}^2) + \frac{1}{2}(x^2 + y^2) + \frac{1-\mu}{r_1} + \frac{\mu}{r_2} \tag{2.7}$$

Setting the velocity components to zero in the equation reveals information regarding where the vehicle may travel in reference to its Jacobi constant. Furthermore, plotting this information exposes the zero-velocity curve, which serves as a limiting boundary whereby vehicles cannot cross unless their Jacobi constant value is below that of the value of the contour. When a vehicle's Jacobi constant is above the mentioned threshold, its velocity will decrease when approaching the curve before it reaches zero. In order to cross, an external force will have to be applied, thus lowering the vehicle's Jacobi constant. Using this concept, it can be demonstrated that a spacecraft has been captured by a planetary body through plotting of the Jacobi constant's zero-velocity curve. Figure 2.2 exhibits examples of zero-velocity curves for multiple Jacobi constants in the Earth-Moon system studied in this paper.

2.2. COORDINATE CONVERSION

Because there are two frames referenced in this study it is necessary to define the transformation between them for kinematic conversions of position and velocity. The initial spacecraft states are given in terms of and with respect to the Earth-centered inertial frame (^{i}) and often are needed in terms of the barycentric synodic frame (^{s}). The position vector,

defined from the barycenter ($_b$) to the spacecraft ($_{sc}$), is expressed in terms of the inertial frame in equation 2.8 and in terms of the synodic frame in equation 2.9, as shown in Figure 2.3.
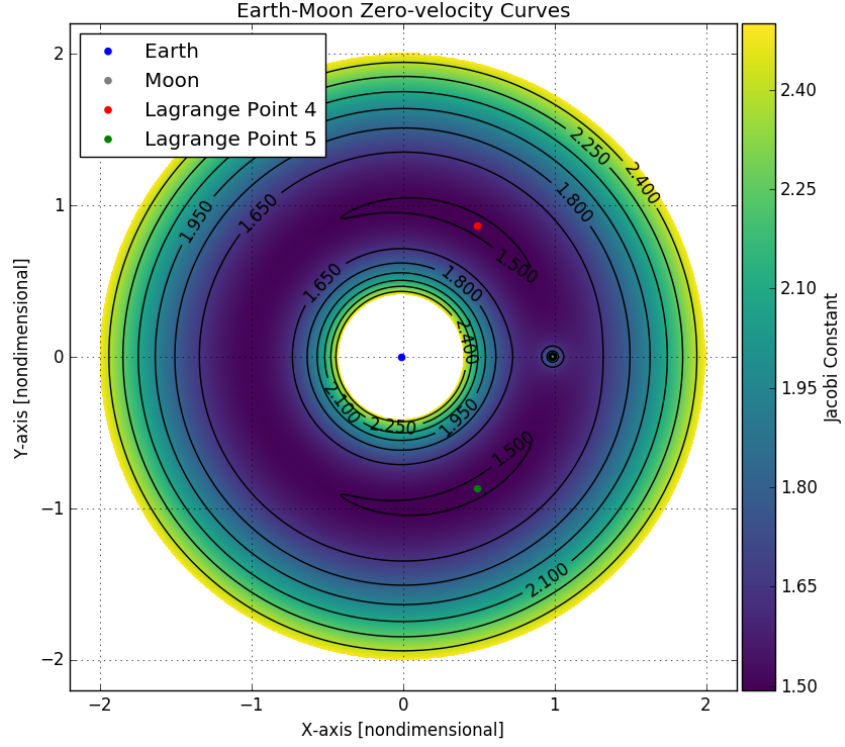
Figure 2.2. Zero-velocity contours (curves) and respective Jacobi constant values for the Earth-Moon System.

$$^i\vec{\rho} = {}^i\vec{r}_{sc} - {}^i\vec{r}_b = \alpha_{sc_1}\hat{X} + \alpha_{sc_2}\hat{Y} + \alpha_{sc_3}\hat{Z} - (\alpha_{b_1}\hat{X} + \alpha_{b_2}\hat{Y} + \alpha_{b_3}\hat{Z}) \tag{2.8}$$

$$^s\vec{\rho} = {}^s\vec{r}_{sc} - {}^s\vec{r}_b = \beta_{sc_1}\hat{x} + \beta_{sc_2}\hat{y} + \beta_{sc_3}\hat{z} - (\beta_{b_1}\hat{x} + \beta_{b_2}\hat{y} + \beta_{b_3}\hat{z}) \tag{2.9}$$

From here a simple rotation using a direction cosine matrix, using equation 2.10, will allow conversion of the position vector from the inertial frame to the synodic frame

$$^s\vec{\rho} = A_{is}{}^i\vec{\rho} \tag{2.10}$$
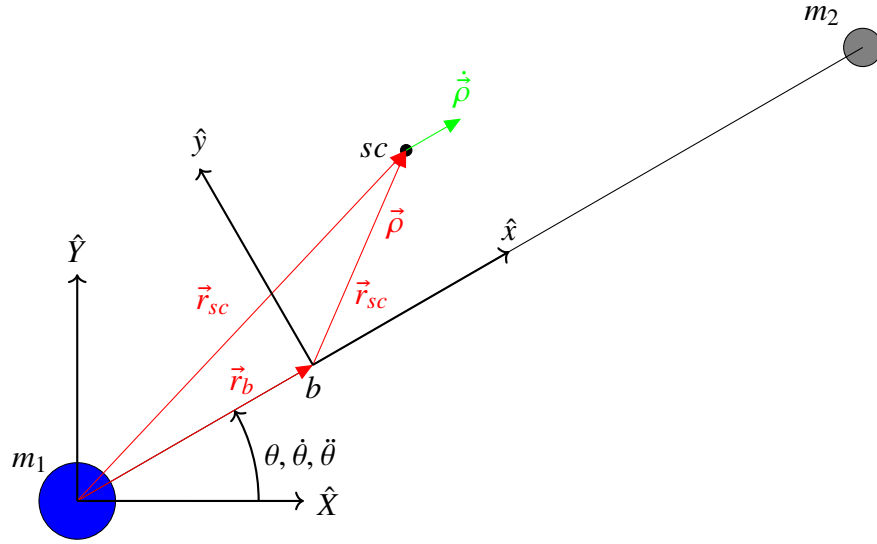
Figure 2.3. Position and velocity vectors associated with conversion between the Earth-centered inertial ($\hat{X}$, $\hat{Y}$, $\hat{Z}$) and barycentric synodic ($\hat{x}$, $\hat{y}$, $\hat{z}$) frames.

where A_{is} is defined by the unit-column vectors of the lunar position, normal, and specific angular momentum and then transposed; as shown in equation 2.11 with angular momentum defined in equation 2.12.

$$A_{is} = \left[\frac{^i\vec{r}_{moon}}{||^i\vec{r}_{moon}||} \quad \frac{^i\vec{h}_{moon}}{||^i\vec{h}_{moon}||} \times \frac{^i\vec{r}_{moon}}{||^i\vec{r}_{moon}||} \quad \frac{^i\vec{h}_{moon}}{||^i\vec{h}_{moon}||} \right]^T \tag{2.11}$$

where

$$^i\vec{h}_{moon} = {^i\vec{r}_{moon}} \times {^i\dot{\vec{r}}_{moon}} \tag{2.12}$$

The vector $^i\vec{\rho}$ and $^s\vec{\rho}$ is then equal in *magnitude* and *direction*, but expressed in terms of different frames [109]. To specify velocity, the inertial derivative is taken of equation 2.9 with respect to time to give

$$\frac{^id}{dt}\vec{\rho} = (\dot{\beta}_{sc_1} - \dot{\beta}_{b_1})\hat{x} + (\dot{\beta}_{sc_2} - \dot{\beta}_{b_2})\hat{y} + (\dot{\beta}_{sc_3} - \dot{\beta}_{b_3})\hat{z}$$
$$+(\beta_{sc_1} - \beta_{b_1})\dot{\hat{x}} + (\beta_{sc_2} - \beta_{b_2})\dot{\hat{y}} + (\beta_{sc_3} - \beta_{b_3})\dot{\hat{z}} \tag{2.13}$$

and then simplified to

$$^i\dot{\vec{\rho}} = {^s_i\dot{\vec{\rho}}} + {^{si}\dot{\vec{\theta}}} \times {^i\vec{\rho}} \tag{2.14}$$

where

$$^{i}\dot{\vec{\rho}} = {}^{i}\dot{\vec{r}}_{sc} - {}^{i}\dot{\vec{r}}_{b} \tag{2.15}$$

and

$$^{s}_{i}\dot{\vec{\rho}} = A_{is}^{T}\,{}^{s}\dot{\vec{\rho}} \tag{2.16}$$

Equation 2.14 gives the velocity relationship between the Earth-centered inertial frame and barycentric synodic frame with $^{si}\dot{\vec{\theta}}$ being the angular velocity of the synodic frame with respect to the inertial frame. The velocity with respect to the synodic frame in terms of the inertial frame is $^{s}_{i}\dot{\vec{\rho}}$; meaning that the direction cosine matrix should be applied to the velocity with respect to the synodic frame, as shown in equation 2.16. Rearranging equation 2.14 and substituting into equation 2.9 to solve for the spacecraft velocity with respect to the synodic frame *and* in terms of the synodic frame gives

$$^{s}\dot{\vec{r}}_{sc} = {}^{i}_{s}\dot{\vec{\rho}} - A_{is}({}^{si}\dot{\vec{\theta}} \times {}^{i}\vec{\rho}) + {}^{s}\dot{\vec{r}}_{b} \tag{2.17}$$

where

$$^{i}_{s}\dot{\vec{\rho}} = A_{is}\,{}^{i}\dot{\vec{\rho}} \tag{2.18}$$

with $^{s}\dot{\vec{r}}_{b}$ being a zero vector for the CR3BP and $^{i}_{s}\dot{\vec{\rho}}$ the inertial velocity expressed in terms of the synodic frame.

The angular velocity vector is calculated by scaling the Moon's specific angular momentum vector to the synodic frame's angular velocity with respect to the inertial. The angular velocity of the synodic frame is computed using equation 2.19 where G is the universal gravitational constant and M^{*} is the characteristic mass. It is now possible to calculate the angular velocity vector of the synodic frame with respect to the inertial frame for the CR3BP, as

$$^{si}\dot{\theta} = \sqrt{\frac{GM^*}{||^i\vec{r}_{moon}||^3}} \qquad (2.19)$$

$$^{si}\dot{\vec{\theta}} = {}^{si}\dot{\theta}\frac{^i\vec{h}_{moon}}{||^i\vec{h}_{moon}||} \qquad (2.20)$$

2.3. HIGH-FIDELITY MODELS

High-fidelity models play a vital role in accurately computing the trajectory of a spacecraft, and usually include modeling thruster performance, propellant tanks, and spacecraft mass to simulate finite and impulsive burns [111, 112, 113]. Although the CR3BP allows insight on a spacecraft's trajectory when considering the gravity fields of the Earth and Moon, high-fidelity models can provide more detailed information of a spacecraft's trajectory with respect to a wider variety of perturbations, such as atmospheric drag, solar radiation pressure, and gravitational potential. Despite the fact that satellites operate in the vacuum of space, atmosphere around a celestial body, such as the Earth, can induce drag on the vehicle and decay its orbit [109]. Additionally, solar radiation pressure is a force applied to the spacecraft by the exchange of momentum between it and solar photons [114]. Finally, third-body forces include the gravitational force from additional celestial bodies not located within the immediate vicinity of the spacecraft; with respect to this research, this includes the Sun and Jupiter, which are the most massive objects in the solar system and have significant effects on motion within the Earth-Moon system. Furthermore, the masses of the Earth and Moon are not simple point masses as they are not truly spherically shaped, which poses further limitations of the CR3BP [109, 112, 113]. For this reason, gravitational potential models, such as spherical harmonics and solid tides, can be applied for a more accurate representation. Incorporating these perturbations into the simulation can provide a more realistic simulation of a satellite's trajectory.

The aforementioned perturbations are part of a simulation which propagates a trajectory with respect to time utilizing a fixed or variable step size propagator [111, 112, 113]. Some common propagators include Runge-Kutta 4, Runge-Kutta 7, Bulirsch-Stoer, and Keplerian. Many software solutions also exist to provide a high-fidelity model, some of which include a.i. solutions's FreeFlyer, AGI's Systems Tool Kit (STK), and NASA's General Mission Analysis Tool (GMAT) [111, 112, 115]. Targeting and optimization are built into these programs with routines such as differential correction, Newton's Method, and Broyden's Method to help design trajectories through targeting values and locating minimum or maximum values [111, 112, 113].

3. ANALYSIS AND APPROACH

The CR3BP model was used to assess Earth-to-Moon direct-transfer trajectories with CubeSats following the parameters outlined by NASA's Cube Quest Challenge. The Cube Quest Challenge is a competition for launching CubeSats on EM-1 to a direct-transfer lunar trajectory. Although the parameters of the Cube Quest Challenge were employed for the scope of this study as it provides the necessary framework, it is noted that other scenarios also implementing direct-transfer lunar trajectories can benefit from the process outlined below by modifying the relevant parameters.

3.1. CUBE QUEST CHALLENGE PARAMETERS

NASA's Cube Quest Challenge limits CubeSats to 6U and 8 kg [116]. A lunar capture orbit is further defined as having a perilune altitude greater than or equal to 300 km and an apolune radius no greater than 10,000 km [116]. The target orbit in this study is defined at the limits of these parameters as it likely offers the minimum amount of ΔV necessary to meet the requirement. An equatorial lunar radius of 1738.1 km is then used to compute a perilune distance [117]. NASA also provided the following initial parameters in Tables 3.1, 3.2, and 3.3 at disposal from the ICPS, which are specified in the Earth-Centered Inertial (ECI) frame and based on the J2000 epoch [118].

Table 3.1. Six classical orbital elements for CubeSat state at the point of disposal [118].

Classical Elements	
Semimajor axis	2.059547723265584E+05 km
Eccentricity	9.667080033831439E-01
Inclination	2.860654780031044E+01°
Right Ascension of the Ascending Node	6.595689658822360E+01°
Argument of Perigee	4.791616744206894E+01°
True Anomaly	1.224710758805222E+02°

Table 3.2. CubeSat position (x, y, z) and velocity ($\dot{x}$, $\dot{y}$, $\dot{z}$) in the ECI frame at the point of disposal [118].

Cartesian	
x	-1.501540312811781E+04 km
y	-2.356897680091111E+04 km
z	2.241504923500546E+03 km
$\dot{x}$	-4.855378922082240E-01 km/s
$\dot{y}$	-5.048763191594085E+00 km/s
$\dot{z}$	-8.799883161637991E-01 km/s

Table 3.3. Epoch of ICPS disposal [118].

Time in Barycentric Dynamical Time	
Julian Date	0.24581031227118D+07
Calendar Date	Dec 15, 2017 14:56:42.2

Using the date and time information NASA provided for the disposal state, the Moon's state can be estimated using Jet Propulsion Laboratory's (JPL) HORIZONS system. Table 3.4 shows the Moon's state at the same time as disposal within the ECI frame and based on the J2000 epoch [119]. The CR3BP is initialized using this state with the assumption of circular motion.

Table 3.4. Lunar position (x, y, z), velocity ($\dot{x}$, $\dot{y}$, $\dot{z}$), light time, range, and range rate in the ECI frame at the point of disposal [119].

Cartesian	
x	-1.552407596013646E-03 AU
y	-2.187676986451931E-03 AU
z	2.366062230266094E-04 AU
$\dot{x}$	4.517328896775049E-04 AU/day
$\dot{y}$	-3.392941614662592E-04 AU/day
$\dot{z}$	-6.068257361013148E-06 AU/day
Light Time	1.555307779820265E-05 day
Range	2.692931942323680E-03 AU
Range Rate	1.468907226968834E-05 AU/day

3.2. TRAJECTORY CALCULATION METHOD

Each $\Delta \vec{v}$ is calculated in terms of the velocity, normal, binormal (VNB) frame which is defined by NASA in the GMAT User Guide R2016a [120] and allows the direct translation of maneuvers in the CR3BP to the GMAT high-fidelity simulation. This frame has the first principle axis, $\hat{V}$, aligned with the inertial velocity vector with respect to the Moon before the applied $\Delta \vec{v}$. The second axis, $\hat{N}$, is defined by the cross product of the position vector and velocity vector of the spacecraft with respect to the Moon normalized to a unit vector. The final axis completes the right-handed rule with normal crossed by velocity. This is sometimes referred to as the NTW frame as well will $\vec{T}$ aligned with the velocity vector, $\vec{W}$ aligned with the orbit normal, and $\vec{N}$ within the orbit plain and completing the right-hand rule [109].
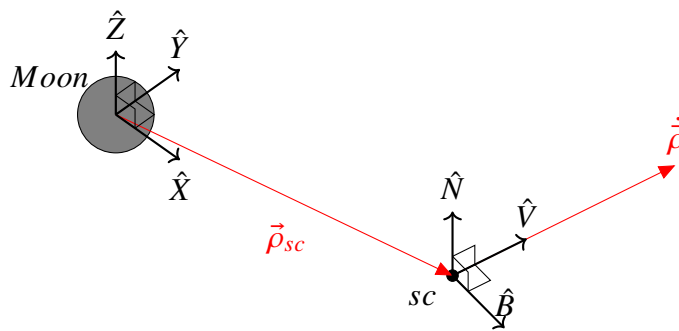
Figure 3.1. The spacecraft local VNB frame defined by its position and velocity with respect to the Moon.

These are defined in equations 3.1, 3.2, and 3.3 where ${}^{i}\vec{\rho}_{sc}$ and ${}^{i}\dot{\vec{\rho}}_{sc}$ represent the spacecraft's inertial position and velocity, and ${}^{i}\vec{\rho}_{moon}$ and ${}^{i}\dot{\vec{\rho}}_{moon}$ represent the Moon's inertial position and velocity.

The direction of each $\Delta \vec{v}$ is initially aligned with the velocity axis, either in the negative or positive direction, depending on the intent of the burn. Next, two rotations are applied to change the direction of the burn. The first rotation, ϕ, is about the normal axis

and the second rotation, θ, is about the velocity axis as show in Figure 3.2. This allows the $\Delta\vec{v}$ direction to be specified along any direction using two variables instead of three for a unit vector.

$$\vec{V} = \frac{^{i}\dot{\vec{\rho}}_{sc} - ^{i}\dot{\vec{\rho}}_{moon}}{||^{i}\dot{\vec{\rho}}_{sc} - ^{i}\dot{\vec{\rho}}_{moon}||} \tag{3.1}$$

$$\vec{N} = \frac{^{i}\vec{\rho}_{sc} - ^{i}\vec{\rho}_{moon}}{||^{i}\vec{\rho}_{sc} - ^{i}\vec{\rho}_{moon}||} \times \vec{V} \tag{3.2}$$

$$\vec{B} = \vec{V} \times \vec{N} \tag{3.3}$$
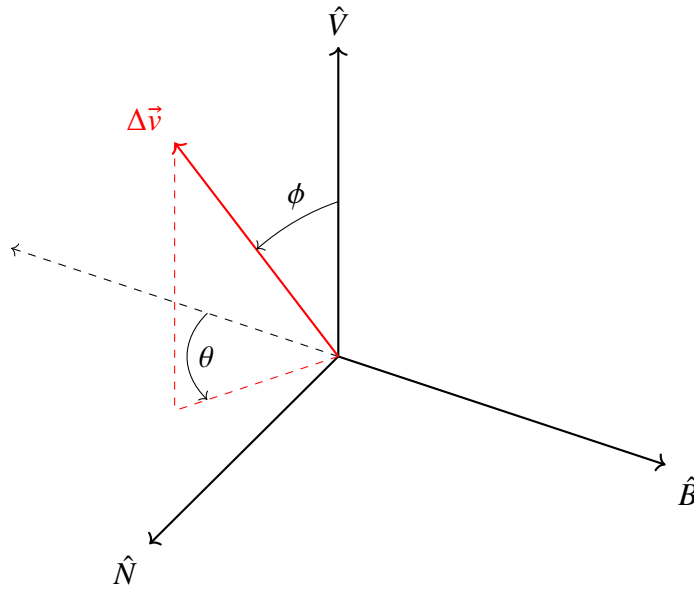
Figure 3.2. The $\Delta\vec{v}$ direction rotations specified by ϕ and θ in the VNB frame.

3.3. APPROACH

The vehicle is initially integrated with the ICPS and injected on a prograde flyby of the Moon, whereby maneuvers are applied to place the vehicle into the targeted orbit. The majority of micropropulsion systems flown and developed for CubeSats are finite-burn systems; therefore, focus was placed on finite-burn trajectories as the available hardware

is more frequently used and mature than continuous-thrust systems [35]. Five different scenarios were analyzed to determine the potential for achieving lunar capture using a combination of maneuvers at various locations including disposal, the edge of the outer Van Allen radiation belt, and perilune. A maneuver at the disposal position would take place at the initial state from which the CubeSat is deployed from the ICPS. Alternatively, a maneuver occurring at the position of the edge of the Van Allen radiation belt occurs when the vehicle first crosses an Earth altitude of 36,000 miles (64,307.384 km) from the center of the Earth. Finally, the maneuver at the perilune position occurs at the point at which the trajectory is closest to the center of the Moon.

1. Illustrated in Figure 3.3, the vehicle is disposed from the ICPS and coasts to perilune, where it will perform a burn to achieve lunar capture in the near anti-velocity direction (Perilune 1).
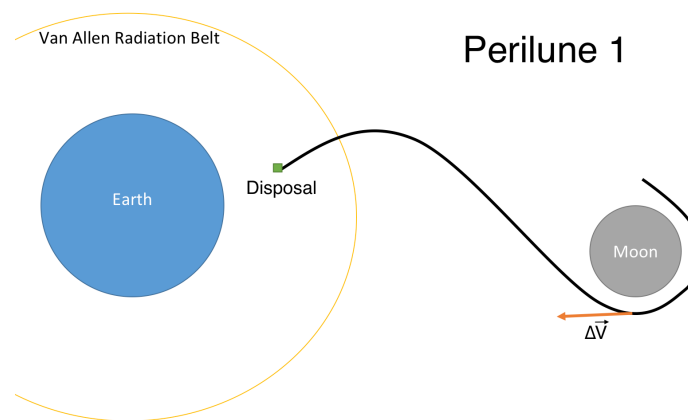
Figure 3.3. An illustration of Perilune 1.

2. The vehicle performs its first maneuver immediately following disposal from the ICPS to decrease the lunar flyby altitude and coasts to perilune where it will perform a burn to achieve lunar capture in the near anti-velocity direction (Disposal 1), shown in Figure 3.4.
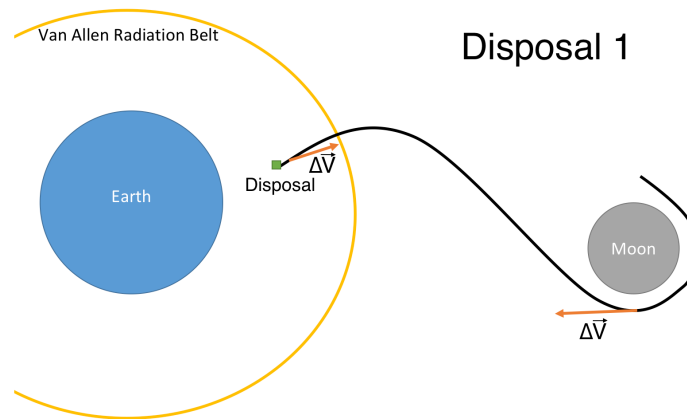
Figure 3.4. An illustration of Disposal 1.

3. The vehicle performs its first maneuver immediately following disposal from the ICPS to target a retrograde flyby of the Moon and coasts to perilune where it will perform a burn to achieve lunar capture in the near anti-velocity direction (Disposal 2), shown in Figure 3.5.
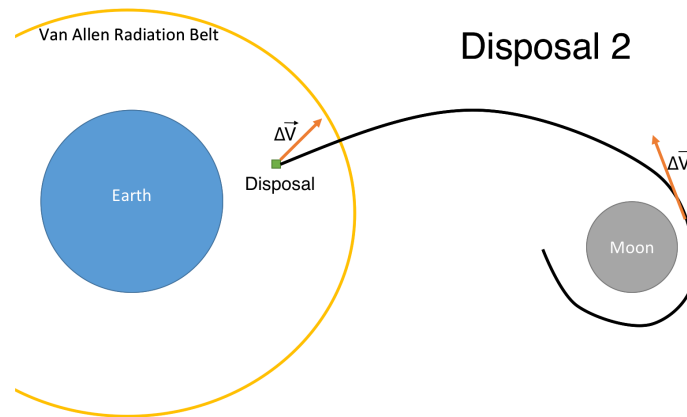
Figure 3.5. An illustration of Disposal 2.

4. Illustrated in Figure 3.6, the vehicle is disposed from the ICPS and coasts to the outer edge of the Van Allen belt where it will perform a maneuver to decrease the lunar flyby altitude. It coasts again to perilune where it will perform a burn to achieve lunar capture in the near anti-velocity direction (Van Allen 1).
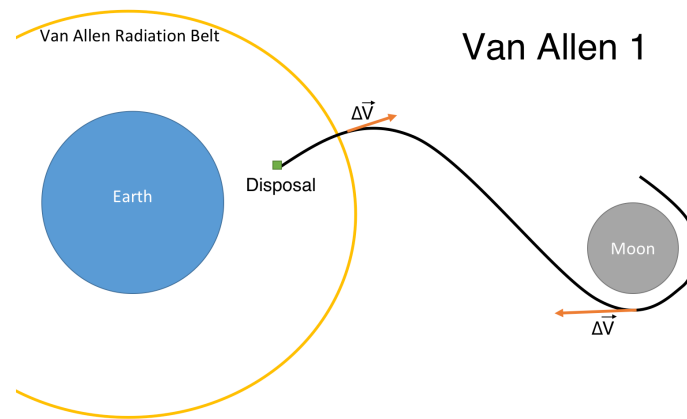
Figure 3.6. An illustration of Van Allen 1.

5. The vehicle is disposed from the ICPS and coasts to the outer edge of the Van Allen belt where it will perform a maneuver to target a retrograde flyby of the Moon. It coasts again to perilune where it will perform a burn to achieve lunar capture in the near anti-velocity direction (Van Allen 2), displayed in Figure 3.7.
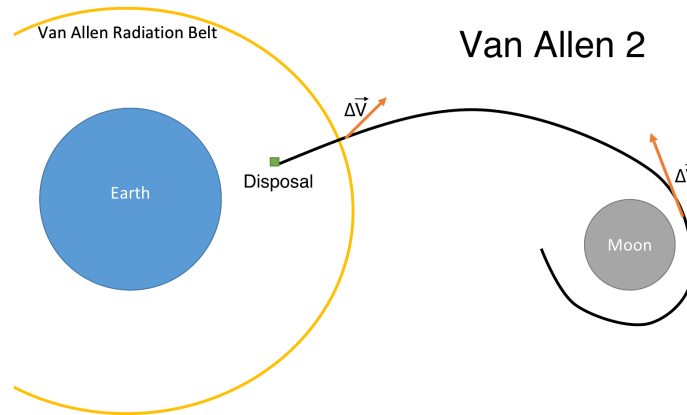

Figure 3.7. An illustration of Van Allen 2.

Each trajectory was selected to provide a realistic scenario for a CubeSat lunar mission. Perilune 1 reduces trajectory complexity as it is the simplest design with a single burn at perilune. Adding an additional burn as early as possible in the trajectory may provide a more fuel-efficient design, which is the premise for Disposal 1 and Disposal 2. However, in both of the Disposal scenarios, the CubeSat remains in an "on" state while traveling

through the outer Van Allen radiation belt. CubeSats are less likely to have radiation-hardened avionics hardware compared to traditional satellites due to their expensive cost, and therefore traveling through the Van Allen radiation belt can be a risk to mission success. To mitigate this, Van Allen 1 and Van Allen 2 were considered as the small spacecraft may be left in an "off" state until outside the radiation belt and then offered the first opportunity for a trajectory maneuver. Finally, retrograde trajectories, Disposal 2 and Van Allen 2, were additionally considered because they offer an added benefit as the vehicle is not lost into deep space, beyond communication limits, should the maneuver at perilune fail. Instead, the spacecraft would return back in the general direction of Earth, potentially offering an opportunity to salvage the mission.

This investigation was accomplished through constructing the aforementioned scenarios in the CR3BP in order to ascertain their effectiveness in preliminary mission design. The CR3BP model was coded in Python and propagation accuracy tested using arbitrary combinations of position and velocity, as shown in Table 3.5, to ensure the Jacobi Integral remained constant throughout the maneuver-less flights via Equation 2.7. The disposal state acquired from NASA was then converted into the synodic frame using two equations, 2.9 and 2.17, and propagated in the coded model.

Table 3.5. Jacobi Integral results for three tests of randomly sampled nondimensional (nd) position and velocity across the nondimensional time unit of 10. The difference is absolute value between the starting and ending Jacobi Integral values.

Test Values	Test #1	Test #2	Test #3
x [nd distance]	0.2	0.4	-0.1
y [nd distance]	0.3	0.2	-0.7
z [nd distance]	-0.6	0.2	-0.1
$\dot{x}$ [nd velocity]	-0.1	-0.3	-0.2
$\dot{y}$ [nd velocity]	-0.1	-0.5	0.5
$\dot{z}$ [nd velocity]	-0.1	0.3	0.8
Time [nd time]	10.0	10.0	10.0
Starting Jacobi Integral	1.465800	1.879846	1.180737
Ending Jacobi Integral	1.465800	1.879846	1.180737
Jacobi Integral Difference	4.889666e-11	3.308414e-10	1.589151e-11

For all scenarios, an automatic variant of the Livermore Solver for Differential Equations (LSODE), known as LSODA, was used to propagate the trajectory within the CR3BP with respect to time. LSODA is discussed further in Appendix 1 [121]. In order to propagate forward in time and stop at perilune or apolune, it was necessary to build in an extremum finder, such as the golden-section search technique used here [122]. This was embedded within the secant method, an open root-finding algorithm, to calculate the necessary ΔV magnitude for targeting a specific perilune or apolune target distance [122]. Finally, the Nelder-Mead simplex method is a multidimensional minimization function and was used to evaluate the total ΔV by adjusting burn orientations [123]. These methods are discussed in further detail in Appendix B.

Since the burn for Perilune 1 is often modeled as a Hohmann transfer, the burn angle, ϕ, was sampled with a range of 0 and 5 degrees while θ was varied between 0 and 360 degrees for a total of 407 times around perilune with a targeted apolune of 10,000 km. The most efficient burn direction sampled in terms of ΔV was then used as an initial estimate for the Nelder-Mead minimization function to find the global minimum of ΔV for this trajectory design.

The process for finding efficient burns for Disposal 1 and Van Allen 1 included sampling the burn orientations at disposal and perilune separately. The disposal burns targeted a 300 km perilune altitude while the perilune or second burn targeted a 10,000 km apolune distance. First, the disposal burn was sampled 962 times for Disposal 1 and 777 times for Van Allen 1 in various directions while the second burn orientation was held constant with an anti-velocity burn direction. Because of the lunar proximity at perilune, the optimal direction of the second burn is similar to a Hohmann transfer. This means the anti-velocity direction is an appropriate initial estimate for use in these simulations. Next, the sample that produced the lowest total ΔV was held constant while the maneuver at perilune (second burn) was directionally varied and sampled 407 times, again with a target apolune of 10,000 km. The second burn orientation sample that produce the minimum total

ΔV was then used in conjunction with the first burn sample result to prime the Nelder-Mead minimization function and find the combination of burns that produce a global minimum of total ΔV.

The retrograde direction followed a similar process for both Disposal 2 and Van Allen 2; however, the initial ΔV magnitude estimates for the first burn were increased to target a retrograde perilune. Both scenarios sampled 777 directions for the first burn and 407 directions for the second burn.

After obtaining the most efficient maneuvers for all five scenarios, the zero-velocity curve was plotted in the synodic frame using each scenario's final Jacobi constant to confirm the spacecraft will stay within the lunar vicinity.

To evaluate their effectiveness in preliminary mission design, the maneuvers defined by locations (disposal, edge of the Van Allen belt, and perilune) and VNB ΔV were simulated with the GMAT high-fidelity model containing the Joint Earth Gravity Model-2, a lunar point mass, and utilizing RungeKutta89 for the integrator. The maneuvers in GMAT were then set to target the same lunar distance as the previously discussed Python CR3BP model by varying the change in velocity along each axis in the VNB frame.

4. RESULTS AND DISCUSSION

Using the methods outlined in the above sections, five different scenarios (Perilune 1, Disposal 1, Disposal 2, Van Allen 1, Van Allen 2) were analyzed to determine the ΔV requirements for lunar capture. Prior to discussing the results of these scenarios, a ballistic trajectory (i.e. without maneuvers applied after ICPS disposal) was propagated in order to provide a reference. All trajectory maneuvers discussed in this section are applied using the spacecraft's lunar velocity, normal, bi-normal (VNB) frame as described in Section 3.2.

4.1. BALLISTIC TRAJECTORY

The spacecraft reached perilune at 97.467 hours following disposal with a radial distance of 3408.722 km. As demonstrated by Figure 4.1, when the spacecraft was disposed from the ICPS it was en route for a flyby of the Moon. Calculating the Jacobi constant results in a value of 1.142379, which is below the minimum zero-velocity value for the system located at Lagrange Points 4 and 5. It is noted that the inertial frame views of the spacecraft's ballistic trajectory can be found in Appendix A Figure 1.
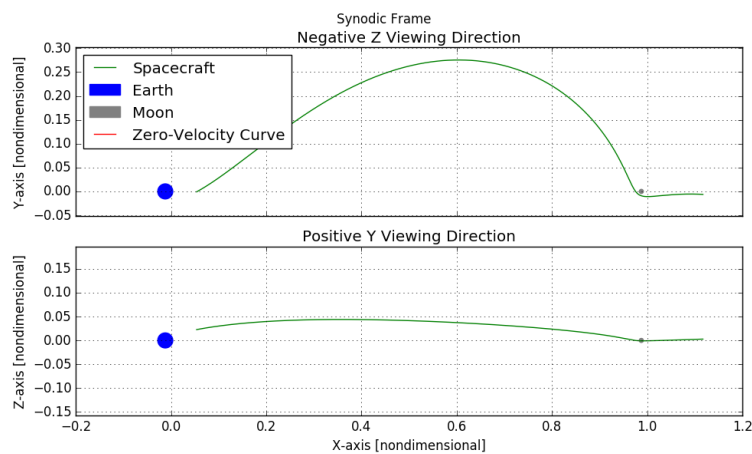

Figure 4.1. The ballistic trajectory beginning at disposal from the ICPS and viewed in the synodic frame of the Earth-Moon system.

Viewing this trajectory in a high-fidelity simulator, such as GMAT, provided slightly different results. GMAT showed the spacecraft reaching perilune at 101.519 hours with a distance of 4034.070 km. This is a difference of 4.052 hours and 625.348 km when compared to the CR3BP results. For comparison, similar high-fidelity views of the above trajectory are included in Figures 4.2 and 4.3.
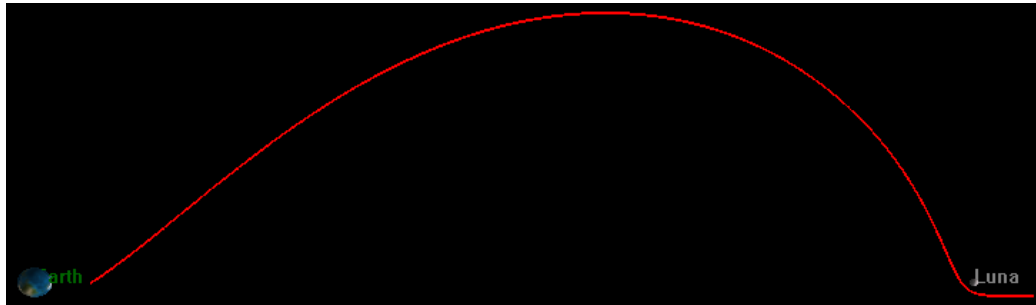
Figure 4.2. The ballistic trajectory simulated in GMAT, beginning at disposal from the ICPS, and viewed along the negative Z direction of the X-Y projection of the Earth-Moon rotating frame.
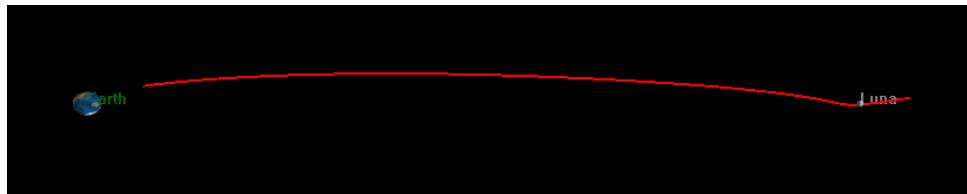
Figure 4.3. The ballistic trajectory simulated in GMAT, beginning at disposal from the ICPS, and viewed along the positive Y direction of the X-Z projection of the Earth-Moon rotating frame.

4.2. PERILUNE 1

The lowest ΔV maneuver determined by the methods previously discussed resulted in a magnitude of 426.683 m/s oriented with a $\phi = 0.108$ degrees and a $\theta = 344.164$ degrees. The result in the VNB frame are show in Table 4.1. Figure 4.4 shows the resulting global minimum of total ΔV with respect to the perilune burn direction.

A Jacobi constant of 1.853585 was calculated, which is above the minimum for the system as indicated in Figure 4.5.
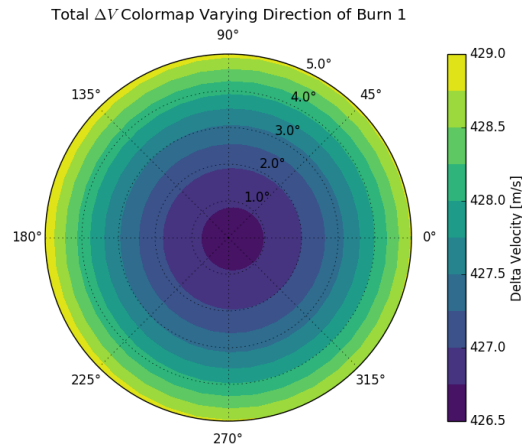
Figure 4.4. Filled contour plot of the total ΔV required for lunar capture with an apolune radial distance of 10,000 km of the burn for Perilune 1. The orientation of the burn was varied with the angle displayed around the perimeter of the plot specifying angular rotation about the velocity vector (θ), while the angle counting up from the center is rotation about the normal vector (ϕ).

Table 4.1. The lowest ΔV found for Perilune 1 in the CR3BP.

Frame Axis	Perilune Burn Velocity [m/s]
Velocity (V)	-426.68190912275477666
Normal (N)	0.21973075074241340
Binormal (B)	0.77467912887630450
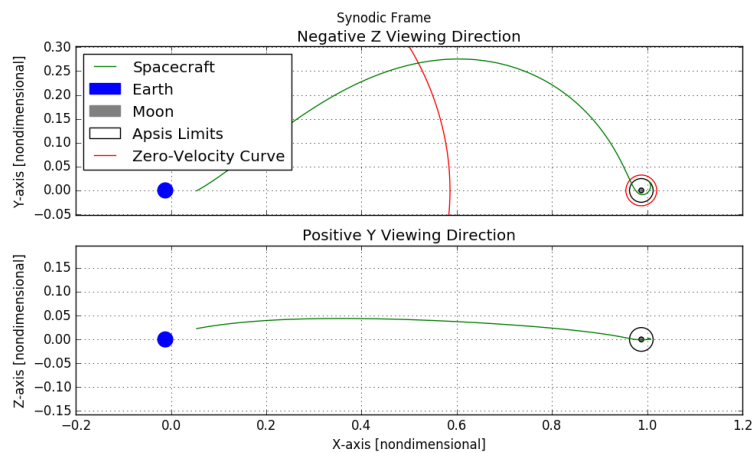
Figure 4.5. The Perilune 1 trajectory beginning at disposal from the ICPS and viewed in the synodic frame of the Earth-Moon system.

Applying the same targets in GMAT for a high-fidelity simulation resulted in a ΔV of 435.531 m/s; a difference of 8.848 m/s. Differences in the perilune time and distance were the same as the ballistic trajectory because the initial conditions are identical. For comparison, similar high-fidelity views of the above trajectory are shown in Figures 4.6 and 4.7.
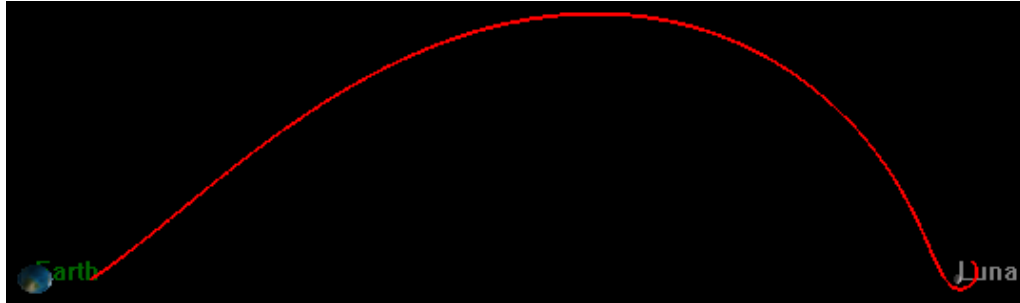
Figure 4.6. The Perilune 1 trajectory simulated in GMAT, beginning at disposal from the ICPS, and viewed along the negative Z direction of the X-Y projection of the Earth-Moon rotating frame.
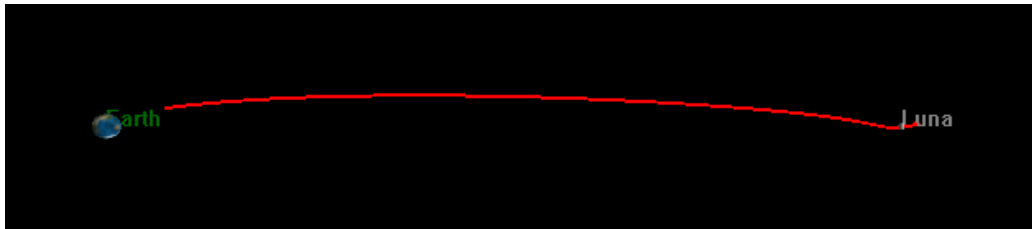
Figure 4.7. The Perilune 1 trajectory simulated in GMAT, beginning at disposal from the ICPS, and viewed along the positive Y direction of the X-Z projection of the Earth-Moon rotating frame.

4.3. DISPOSAL 1 AND DISPOSAL 2

Scenarios in this section utilize a burn following disposal from the ICPS and at perilune as described in Section 3.3.

4.3.1. Disposal 1. The methods described in Section 3.3 determined that the lowest ΔV burn angles for the maneuver at disposal for the prograde direction are $\phi = 17.233$ degrees and $\theta = 147.124$ degrees. Figure 4.8 shows the resulting global minimum of

total ΔV with respect to the disposal burn direction. The magnitude of this maneuver was 1.507 m/s with results in the VNB frame shown in Table 4.2. The increased velocity, when compared to the ballistic trajectory, resulted in the vehicle reaching perilune at 96.869 hours.
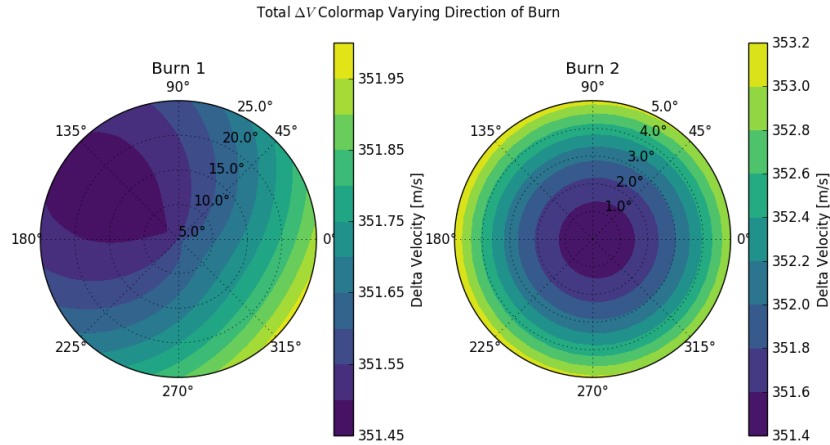

Figure 4.8. Filled contour plots of the total ΔV required for lunar capture into a 2038.1 km by 10,000 km orbit with respect to the direction of the burn for Disposal 1. The angle displayed around the perimeter of the plot specifies angular rotation about the velocity vector (θ), while the angle counting up from the center is rotation about the normal vector (ϕ).

Table 4.2. The lowest ΔV found for Disposal 1 in the CR3BP.

Frame Axis	Disposal Burn Velocity [m/s]	Perilune Burn Velocity [m/s]
Velocity (V)	1.43893748601394561	-349.96639049702510382
Normal (N)	0.24228599375782529	0.00234205188879566
Binormal (B)	0.37486384267088247	0.90298568621253322

The lowest ΔV for the second maneuver, also referenced in Table 4.2, occurred at perilune with a magnitude of 349.968 m/s. It was applied with $\phi = 0.148$ degrees and $\theta = 359.851$ degrees, which is exhibited at the global minimum in Figure 4.8. This resulted in a total ΔV applied by the spacecraft to be 351.474 m/s for lunar capture. A Jacobi constant of 1.892680 was calculated, which is above the minimum for the system as indicated in Figure 4.9.
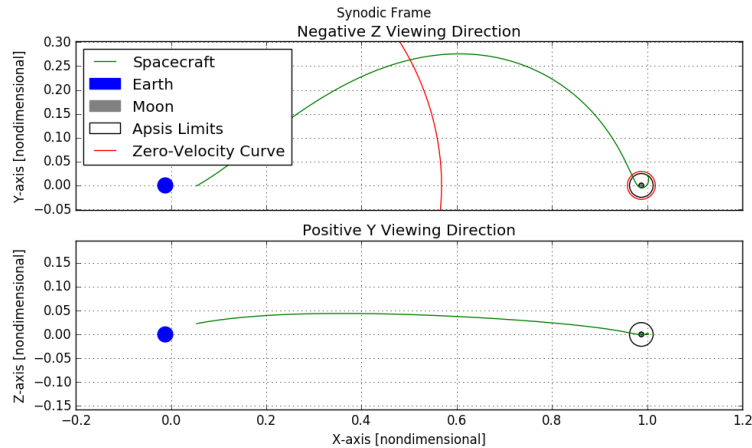
Figure 4.9. The Disposal 1 trajectory beginning at disposal from the ICPS and viewed in the synodic frame of the Earth-Moon system.

Table 4.3. The lowest ΔV found for Disposal 1 in GMAT.

Frame Axis	Disposal Burn Velocity [m/s]	Perilune Burn Velocity [m/s]
Velocity (V)	1.713841149067211	-371.1549047162309
Normal (N)	2.702290898098294	-10.50965507175847
Binormal (B)	0.2503847481528935	-3.734830883419485

Applying the same targets in GMAT for a high-fidelity simulation provided the results in Table 4.3 with a disposal burn magnitude of 3.210 m/s and a perilune burn magnitude of 371.322 m/s. This gives a total ΔV of 374.532 m/s, 23.058 m/s greater than the CR3BP results. Perilune arrival time was 100.682 hours after disposal and 3.813 hours more than CR3BP. High-fidelity views of the above trajectory are included in Figures 4.10 and 4.11.

Figure 4.10. The Disposal 1 trajectory simulated in GMAT, beginning at disposal from the ICPS, and viewed along the positive Y direction of the X-Z projection of the Earth-Moon rotating frame.

Figure 4.11. The Disposal 1 trajectory simulated in GMAT, beginning at disposal from the ICPS, and viewed along the negative Z direction of the X-Y projection of the Earth-Moon rotating frame.

4.3.2. Disposal 2. Optimizing the retrograde direction for a minimum ΔV determined that the optimal burn angles for the maneuver at disposal are ϕ = 18.109 degrees and θ = 162.211 degrees. The magnitude for this maneuver was 10.243 m/s and converting this into the VNB frame resulted in the values listed in Table 4.4. The resulting global minimum of total ΔV with respect to the disposal burn direction is included in Figure 4.12. The increase in velocity resulted in the vehicle reaching perilune at 95.158 hours.
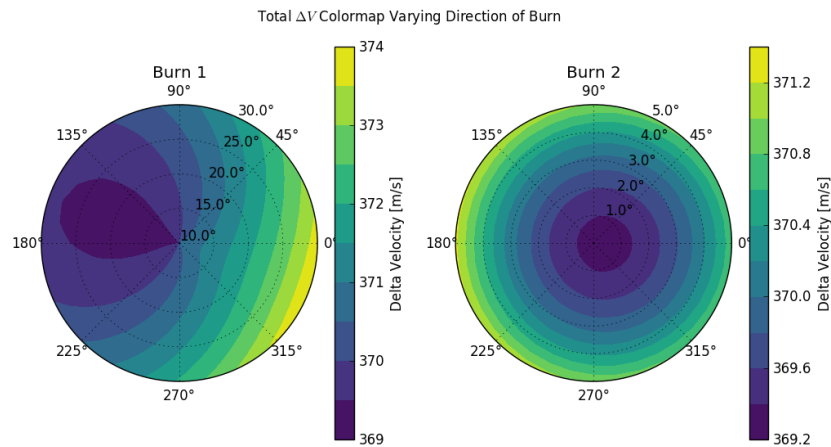
Figure 4.12. Filled contour plots of the total ΔV required for lunar capture into a retrograde 2038.1 km by 10,000 km orbit with respect to the direction of the burn for Disposal 2. The angle displayed around the perimeter of the plot specifies angular rotation about the velocity vector (θ), while the angle counting up from the center is rotation about the normal vector (ϕ).

Table 4.4. The lowest ΔV found for Disposal 2 in the CR3BP.

Frame Axis	Disposal Burn Velocity [m/s]	Perilune Burn Velocity [m/s]
Velocity (V)	9.73604765528207974	-359.07698601697135565
Normal (N)	0.97272972292176702	-0.00283306562453545
Binormal (B)	3.03161335406129401	2.48196707758384589
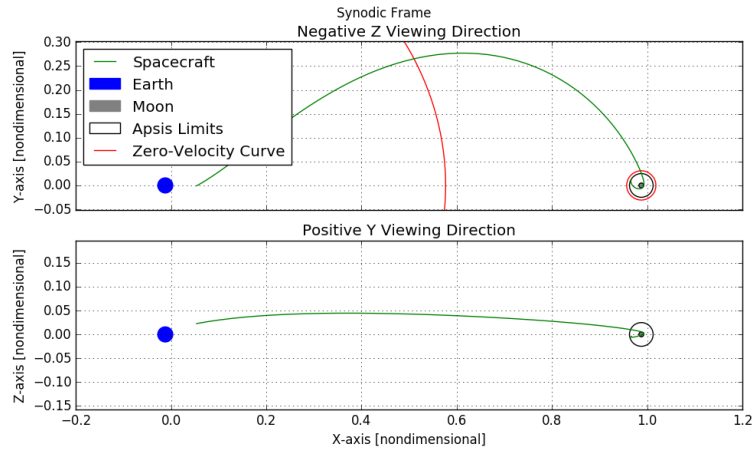
Figure 4.13. The Disposal 2 trajectory beginning at disposal from the ICPS and viewed in the synodic frame of the Earth-Moon system.

The second maneuver is optimal with a magnitude of 359.086 m/s at perilune, $\phi = 0.396$ degrees, and $\theta = 0.065$ degrees. This is referenced in Table 4.4 and in Figure 4.12, which exhibits the global minimum. This resulted in a total ΔV applied by the spacecraft to 369.329 m/s for lunar capture. A Jacobi constant of 1.873412 was calculated, which is above the minimum for the system as indicated in Figure 4.13.

Table 4.5. The lowest ΔV found for Disposal 2 in GMAT.

Frame Axis	Disposal Burn Velocity [m/s]	Perilune Burn Velocity [m/s]
Velocity (V)	9.960039332894962	-367.6209539389422
Normal (N)	0.9953495853268393	1.877250783208875
Binormal (B)	3.071643412008703	-0.5036587120944503

Applying the same targets in GMAT for a high-fidelity simulation provided the results in Table 4.5 with a disposal burn magnitude of 10.470 m/s and a perilune burn magnitude of 367.626 m/s. This gives a total ΔV of 378.096 m/s, 8.767 m/s greater than

the CR3BP results. Perilune arrival time was 98.891 hours after disposal and 3.733 hours more than CR3BP. High-fidelity views of the above trajectory are included in Figures 4.14 and 4.15.
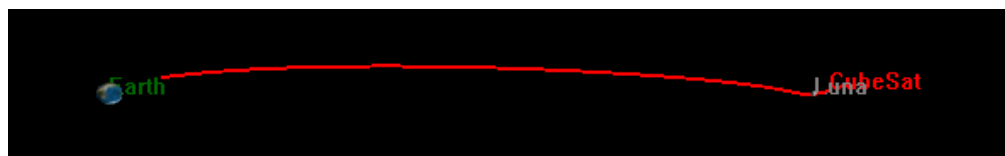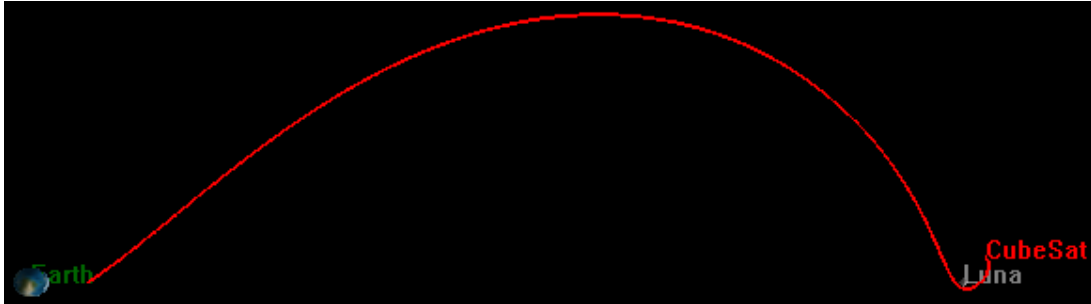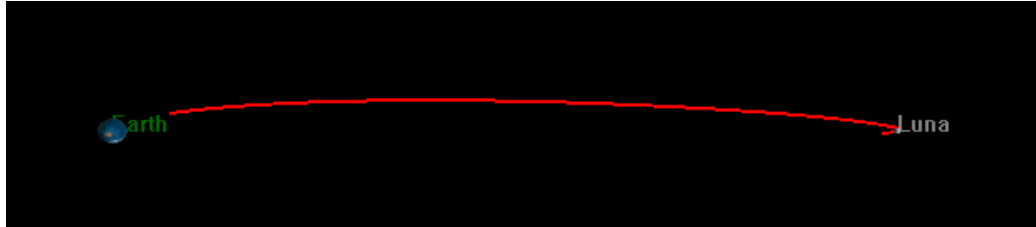

Figure 4.14. The Disposal 2 trajectory simulated in GMAT, beginning at disposal from the ICPS, and viewed along the negative Z direction of the X-Y projection of the Earth-Moon rotating frame.
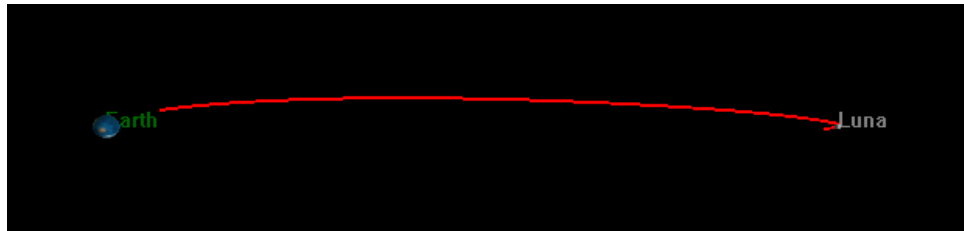
Figure 4.15. The Disposal 2 trajectory simulated in GMAT, beginning at disposal from the ICPS, and viewed along the positive Y direction of the X-Z projection of the Earth-Moon rotating frame.

4.4. VAN ALLEN 1 AND VAN ALLEN 2

Scenarios in this section utilize a burn at the edge of the Van Allen radiation belt and at perilune as described in Section 3.3. The time to reach the edge of the Van Allen radiation belt following disposal from the ICPS was calculated to be 2.810 hours with the CR3BP taking 1.085 seconds longer than GMAT.

4.4.1. Van Allen 1. $\phi = 28.178$ degrees and $\theta = 164.574$ degrees were determined to be the optimal burn angles for the maneuver at the edge of the Van Allen radiation belt. Figure 4.16 shows the resulting global minimum of total ΔV with respect to the disposal

burn direction. The magnitude of this maneuver was calculated to be 2.374 m/s with results in the VNB frame shown in Table 4.6. The vehicle reached perilune in 96.929 hours following disposal.
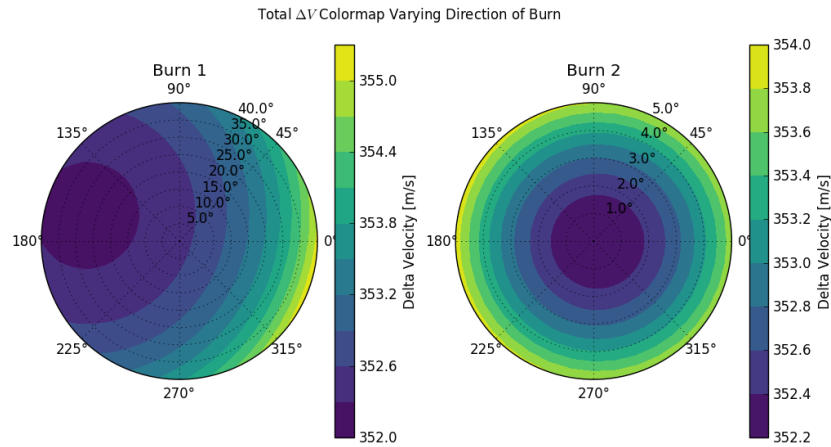
Figure 4.16. Filled contour plots of the total ΔV required for lunar capture into a 2038.1 km by 10,000 km orbit with respect to the direction of the burn for Van Allen 1. The angle displayed around the perimeter of the plot specifies angular rotation about the velocity vector (θ), while the angle counting up from the center is rotation about the normal vector (ϕ).

Table 4.6. The lowest ΔV found for Van Allen 1 in the CR3BP.

Frame Axis	Van Allen Burn Velocity [m/s]	Perilune Burn Velocity [m/s]
Velocity (V)	2.09257616841531692	-349.83572551361441505
Normal (N)	0.29817379620176071	0.00255759754458502
Binormal (B)	1.08063081610241000	0.89734055317542934

The optimal second maneuver, also referenced in Table 4.6, occurred at perilune with a magnitude of 349.837 m/s. It was applied with $\phi = 0.147$ degrees and $\theta = 359.837$ degrees, which is exhibited at the global minimum in Figure 4.16. This resulted in a total ΔV applied by the spacecraft to 352.211 m/s for lunar capture. A Jacobi constant of 1.892679 was calculated following the maneuver at perilune, which is above the minimum for the system as indicated in Figure 4.17.
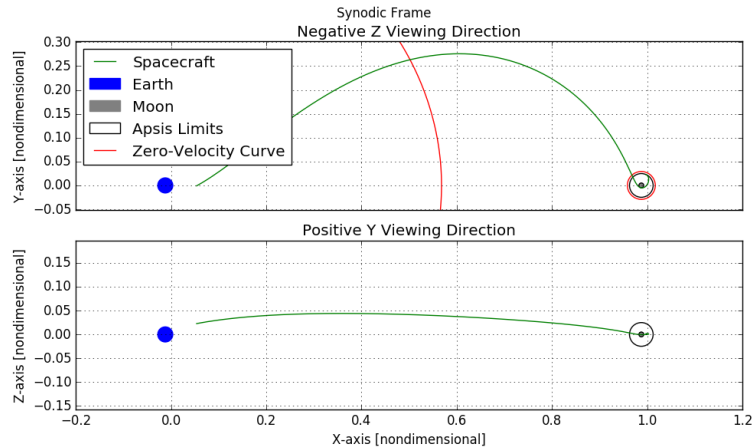
Figure 4.17. The Van Allen 1 trajectory beginning at disposal from the ICPS and viewed in the synodic frame of the Earth-Moon system.

Table 4.7. The lowest ΔV found for Van Allen 1 in GMAT.

Frame Axis	Van Allen Burn Velocity [m/s]	Perilune Burn Velocity [m/s]
Velocity (V)	2.888242648434423	-371.0981193745235
Normal (N)	2.6867827476251	-10.93763310320171
Binormal (B)	0.843519350824362	2.490842595653629

Applying the same targets in GMAT for a high-fidelity simulation provided the results in Table 4.7 with a Van Allen burn magnitude of 4.034 m/s and a perilune burn magnitude of 375.302 m/s. This gives a total ΔV of 375.302 m/s, 23.091 m/s greater than the CR3BP results. Perilune arrival time was 100.709 hours after disposal and 3.780 hours more than CR3BP. High-fidelity views of the above trajectory are included in Figures 4.18 and 4.19.

Figure 4.18. The Van Allen 1 trajectory simulated in GMAT, beginning at disposal from the ICPS, and viewed along the positive Y direction of the X-Z projection of the Earth-Moon rotating frame.

Figure 4.19. The Van Allen 1 trajectory simulated in GMAT, beginning at disposal from the ICPS, and viewed along the negative Z direction of the X-Y projection of the Earth-Moon rotating frame.

4.4.2. Van Allen 2. Optimizing the retrograde direction determined that the optimal burn angles for the maneuver at disposal are $\phi = 29.893$ degrees and $\theta = 178.869$ degrees. Figure 4.20 shows the resulting global minimum of total ΔV with respect to the Van Allen burn direction. The magnitude of this maneuver is 16.218 m/s with results in the VNB frame shown in Table 4.8. After 95.580 hours since disposal, the vehicle reached perilune.
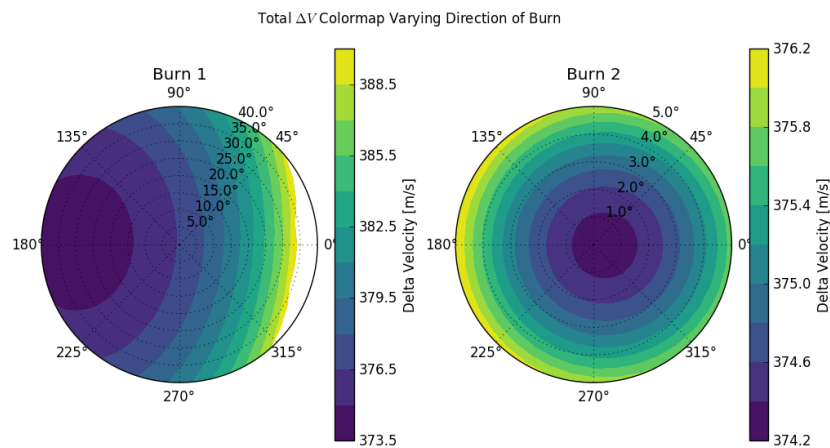
Figure 4.20. Filled contour plots of the total ΔV required for lunar capture into a retrograde 2038.1 km by 10,000 km orbit with respect to the direction of the burn for Van Allen 2. The angle displayed around the perimeter of the plot specifies angular rotation about the velocity vector (θ), while the angle counting up from the center is rotation about the normal vector (ϕ).

As viewed in Table 4.8, the optimal second maneuver occurred at perilune with magnitude 358.083 m/s, and was applied with $\phi = 0.397$ degrees and $\theta = 0.036$ degrees.

This is exhibited at the global minimum in Figure 4.20 and resulted in a total ΔV applied by the spacecraft to 374.302 m/s for lunar capture. A Jacobi constant of 1.873291 was calculated, which is above the minimum for the system as indicated in Figure 4.21.

Table 4.8. The lowest ΔV found for Van Allen 2 in the CR3BP.

Frame Axis	Van Allen Burn Velocity [m/s]	Perilune Burn Velocity [m/s]
Velocity (V)	14.06052540033494610	-358.07472571820075924
Normal (N)	0.15952523112133682	-0.00157624176723490
Binormal (B)	8.08141468952672769	2.48175795037924949
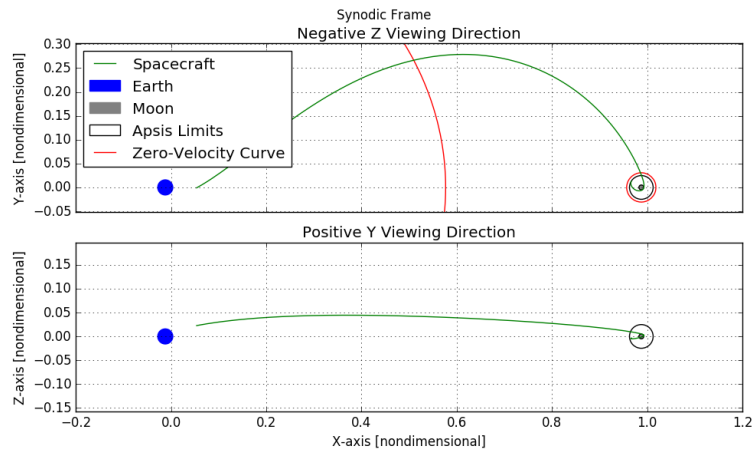
Figure 4.21. The Van Allen 2 trajectory beginning at disposal from the ICPS and viewed in the synodic frame of the Earth-Moon system.

Table 4.9. The lowest ΔV found for Van Allen 2 in GMAT.

Frame Axis	Van Allen Burn Velocity [m/s]	Perilune Burn Velocity [m/s]
Velocity (V)	14.43606477334912	-366.5993416420966
Normal (N)	0.1872737394789262	1.553383948621355
Binormal (B)	8.208905757905184	-0.6401267530754888

Applying the same targets in GMAT for a high-fidelity simulation provided the results in Table 4.9 with a Van Allen burn magnitude of 16.608 m/s and a perilune burn magnitude of 366.603 m/s. This gives a total ΔV of 383.211 m/s, 8.909 m/s greater than

the CR3BP results. Perilune arrival time was 99.362 hours after disposal and 3.862 hours more than CR3BP. High-fidelity views of the above trajectory are included in Figures 4.22 and 4.23.
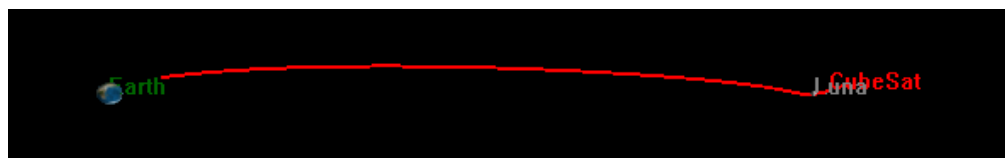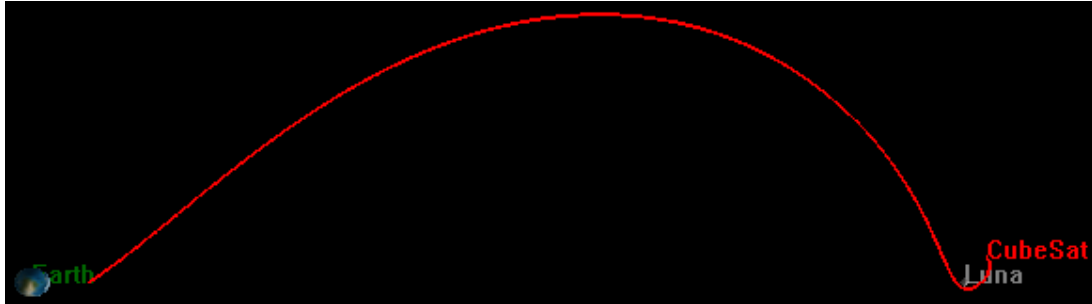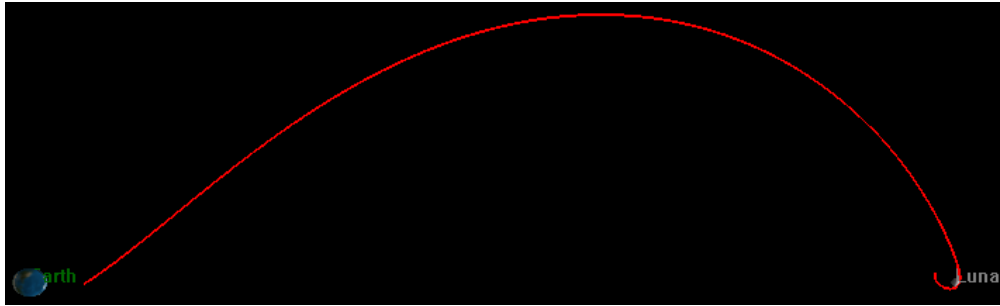

Figure 4.22. The Van Allen 2 trajectory simulated in GMAT, beginning at disposal from the ICPS, and viewed along the negative Z direction of the X-Y projection of the Earth-Moon rotating frame.
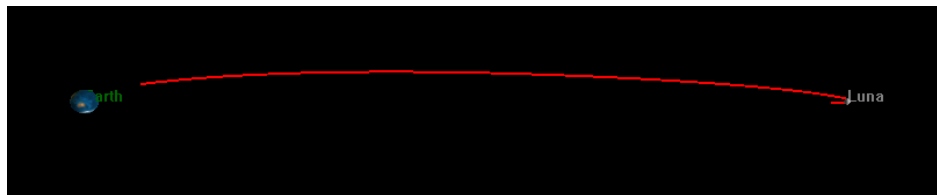
Figure 4.23. The Van Allen 2 trajectory simulated in GMAT, beginning at disposal from the ICPS, and viewed along the positive Y direction of the X-Z projection of the Earth-Moon rotating frame.

4.5. DISCUSSION

The results show that the primary differences between the scenarios in the CR3BP and those in GMAT are travel time and total ΔV. Travel time results are summarized in Table 4.10 and are defined as the length of time between spacecraft disposal from the ICPS and the spacecraft reaching perilune. The travel time in GMAT is consistently 4% longer than in the CR3BP. The reason for this difference is likely due to the circular assumption within the CR3BP whereas GMAT models the Moon's elliptical motion. The Moon's positive range rate in Table 3.4 shows that the Moon is moving away from the Earth as part of its elliptical orbit; therefore, the spacecraft will have to travel farther to reach

perilune in the GMAT simulations. This is the likely cause for the extended travel time in GMAT and explains why the difference is consistent between the trajectory scenarios. Future work could confirm this suspected effect by propagating these orbits with the elliptic restricted three-body problem equations of motion. The total ΔV results are summarized in Table 4.11 with scenarios in GMAT averaging a 4% increase over those in the CR3BP. An explanation for the discrepancy in ΔV between the models may be attributed to the lack of an optimization or minimization routine within GMAT, which would allow for a local minimum of ΔV to be found, thus likely reducing the difference. It is worth noting that the ΔV difference for Disposal 1 and Van Allen 1 is significantly higher than the other three scenarios, which stay between two and three percent. This may imply that early maneuvers in the trajectory are more sensitive to lunar distance for prograde scenarios than retrograde ones.

Table 4.10. Travel time from disposal to perilune for each scenario. Difference is CR3BP time subtracted from GMAT and percent difference is the difference with respect to the CR3BP time. The ballistic trajectory contained matching results with Perilune 1.

Scenario	CR3BP [hrs]	GMAT [hrs]	Difference [hrs]	Difference [%]
Perilune 1	97.467	101.519	4.052	4.157
Disposal 1	96.869	100.682	3.813	3.936
Disposal 2	95.158	98.891	3.733	3.923
Van Allen 1	96.929	100.709	3.780	3.900
Van Allen 2	95.580	99.362	3.782	3.957

Table 4.11. The total ΔV needed for each scenario. The difference is calculated by subtracting the CR3BP value from GMAT's and percentage difference is the difference with respect to CR3BP values.

Scenario	CR3BP [m/s]	GMAT [m/s]	Difference [m/s]	Difference [%]
Perilune 1	426.683	435.531	+8.848	2.074
Disposal 1	351.474	374.532	+23.058	6.560
Disposal 2	369.329	378.096	+8.768	2.374
Van Allen 1	352.211	375.302	+23.091	6.556
Van Allen 2	374.302	383.211	+8.909	2.380

As discussed above, the difference in ΔV between both models may be attributed to the lack of an optimization function within GMAT. Once this is accounted for, one would expect the accuracy at which the CR3BP produces ΔV to be comparable to that which is produced in GMAT. Furthermore, differences in travel time are also comparable, exhibiting only a 4% discrepancy. This, combined with the simplified implementation of the CR3BP when compared to the more complicated models in GMAT make the CR3BP an efficient and effective means of preliminary mission design.

The minimum ΔV requirements displayed in Table 4.11 outline the propulsive needs for lunar capture and range from 351.474 m/s for Disposal 1 to 426.683 m/s for Perilune 1. Multiple propulsion systems are available off-the-shelf that can meet these requirements for an 8.0 kg satellite. The wet mass of VACCO's 3U Lunar Flashlight Propulsion System is 5.0 kg, 2.0 kg of which are dedicated to propellant. Assuming a total wet mass of 8.0 kg, this results in a total available ΔV of 478 m/s, and indicates that satellites 6U and under utilizing this propulsive system are capable of meeting the requirements for all five scenarios discussed. However, due to the large mass and volume of the Lunar Flashlight, it is noted that only 3.0 kg is remaining for other components, which is a significant limitation when choosing this propulsive system and most likely limits the CubeSats using it to 6U or larger. Aerojet Rocketdyne's MPS-130-2U, on the other hand, is contained in a 2U package with a dry mass of 1.4 kg and a fuel mass of 1.4 kg (wet mass of 2.8 kg). It is capable of delivering 380 m/s of ΔV for an 8.0 kg spacecraft, which allows it to achieve all scenarios except for Perilune 1. Busek's BGT-X5 is 1U in volume and capable of accelerating a 4.0 kg CubeSat 146 m/s, which does not meet the minimum ΔV for any scenario; however, limited information is provided by the manufacturer in terms of the system's mass, thus limiting the ability to draw a conclusion regarding the propulsive capabilities for masses less than 4.0 kg. Additionally, the BGT-X5 has the possibility of an increased propellant tank, which may provide the additional propellant necessary to match or exceed the ΔV requirements; however, information is also unavailable from the manufacturer regarding the capacity of

the extended tank and therefore it is not possible to form a conclusion in regards to its ΔV capabilities. Finally, MarCO utilized a cold-gas propellant system that had an estimated max ΔV capability of 318 m/s. Although this CubeSat demonstrated the viability of a small satellite performing in a deep-space mission, it only performed flybys of the Moon and Mars and did not possess a propulsion system capable of meeting the qualifications for lunar capture.

Commonalities were noted among the propulsive systems capable of achieving lunar capture under one or more of the outlined scenarios. All three of the aforementioned propulsive systems utilize green monopropellant that was heated to increase performance. Similar hydrazine-based propulsion systems did not perform as well as the green monopropellant systems. Additionally all three systems are "all-in-one" and include tanks, feed systems, and thrusters.

Although these systems are available off-the-shelf, none have flight heritage and no sources were found demonstrating flown hardware on a CubeSat meeting these performance requirements.

Several limitations of this study open a pathway for future research in providing more detail regarding the use of the CR3BP as a means of preliminary mission design and the propulsive capabilities of CubeSats. First, implementing an optimization routine in GMAT to locate a local minimum of total ΔV would increase the accuracy and provide a better comparison between the CR3BP and GMAT; however, performing this function is not within the scope or time constraints of this research study. Additionally, to provide a more limited scope of study, the propulsion systems are restricted to satellites 6U and under in size and do not include continuous-thrust systems, such as ion thrusters and Hall effect thrusters. Finally, the results are limited to the specifications and guidelines outlined by NASA's CubeQuest Challenge, and therefore, alternative methods of achieving lunar capture with CubeSats may be possible. Because of this, different propulsive technologies may be able to meet the requirements under different parameters.

5. CONCLUSION

The small satellite/CubeSat field is one of the fastest growing means of space exploration, with applications continuing to expand for component development, communication, and scientific research; therefore, it is important to establish suitable Earth-to-Moon direct-transfer trajectories and provide a baseline understanding of their propulsive demands. Using the CR3BP and derived requirements from NASA's Cube Quest Challenge, five different trajectory scenarios were analyzed: Perilune 1 includes a single maneuver at perilune; Disposal 1 and 2, with burns at disposal and perilune; and Van Allen 1 and 2, with burns at the end of the Van Allen belt and perilune. Perilune 2 and Van Allen 2 each utilize a retrograde lunar orbit, while all other aforementioned scenarios are prograde.

This research study was completed to investigate Earth-to-Moon direct-transfer trajectories for small satellites to determine their viability given currently-available micropropulsion systems. The CR3BP was used for this analysis with results compared to those obtained from GMAT in order to determine its effectiveness in preliminary mission design.

Results support the initial hypothesis that the CR3BP is a viable means for preliminary mission design as demonstrated by an average difference of 4% for both time of flight and ΔV when compared to GMAT. Discrepancies in the results are likely attributed to the circular assumption within the CR3BP and the lack of an optimization routine within GMAT. Minimum ΔV requirements for obtaining lunar capture range from 351.474 m/s to 426.683 m/s. Review of literature reveals several off-the-shelf propulsive systems available for meeting these requirements; however, none have flown at the time of this research study.

The CR3BP is an efficient and economical option for preliminary mission design, enabling new projects more opportunity to develop and design without the immediate need for a high-fidelity simulation. This means faster iteration between trajectory designs as the CR3BP requires less resources for development and operation than high-fidelity models.

This allows for quick mission analysis of the viability of potential projects. Furthermore, the ability for clubs, universities, and companies to develop their own mission design tools without the cost of third-party applications reduces the startup cost for new projects and makes them obtainable on a smaller budget. Additionally, satellite design may not require a custom propulsion system for missions demanding higher performance, and off-the-shelf options can dramatically reduce the cost, complexity, and work needed to design a spacecraft, allowing the engineers and scientists to focus resources on other important aspects such as scientific research, education, and component development; however, further work is needed to validate the propulsion technologies for CubeSats in-flight and demonstrate technology readiness.

Several limitations of this study open a pathway for future research in providing more detail regarding the use of the CR3BP as a means of preliminary mission design and the propulsive capabilities of CubeSats. First, implementing an optimization routine in GMAT to locate a local minimum of total ΔV would increase the accuracy and provide a better comparison between the CR3BP and GMAT; however, performing this function is not within the scope or time constraints of this research study. Additionally, to provide a more limited scope of study, the propulsion systems are limited to satellites 6U and under in size and do not include continuous-thrust systems, such as ion thrusters and Hall effect thrusters. Finally, the results are limited to the specifications and guidelines outlined by NASA's CubeQuest Challenge, and therefore, alternative methods of achieving lunar capture with CubeSats may be possible. Because of this, different propulsive technologies may be able to meet the requirements under different parameters.

Because of the limitations within this study, several recommendations in regards to future research are warranted. First a comparison of the CR3BP to GMAT with an optimization routine needs to be done in order to further validate the use of the CR3BP in preliminary mission design. Furthermore, expanding similar research to include other Earth-to-Moon direct-transfer trajectories would further detail the propulsive requirements

necessary for CubeSats to obtain lunar capture under various circumstances. A sensitivity analysis covering uncertainty in the disposal and the ΔV maneuvers would also be beneficial. Additionally, completing a study utilizing the Elliptic Restricted Three Body Problem may provide additional means for preliminary mission design that is not limited by the circular assumption within the CR3BP and may provide a more accurate estimation of propulsive requirements. Similarly, the patched conic method may also be applied and provide a good comparison for use in preliminary mission design versus the CR3BP.

Although, more research regarding the use of the CR3BP with other propulsion types and trajectory scenarios is needed for further clarification, the results of this research study provide a positive outlook for its use in preliminary mission design. Furthermore, the future of lunar-based opportunities for small satellites is possible given currently available propulsion systems.

APPENDIX A.

TRAJECTORY PLOTS

The figures displayed below are supplemental to those shown in Section 4.
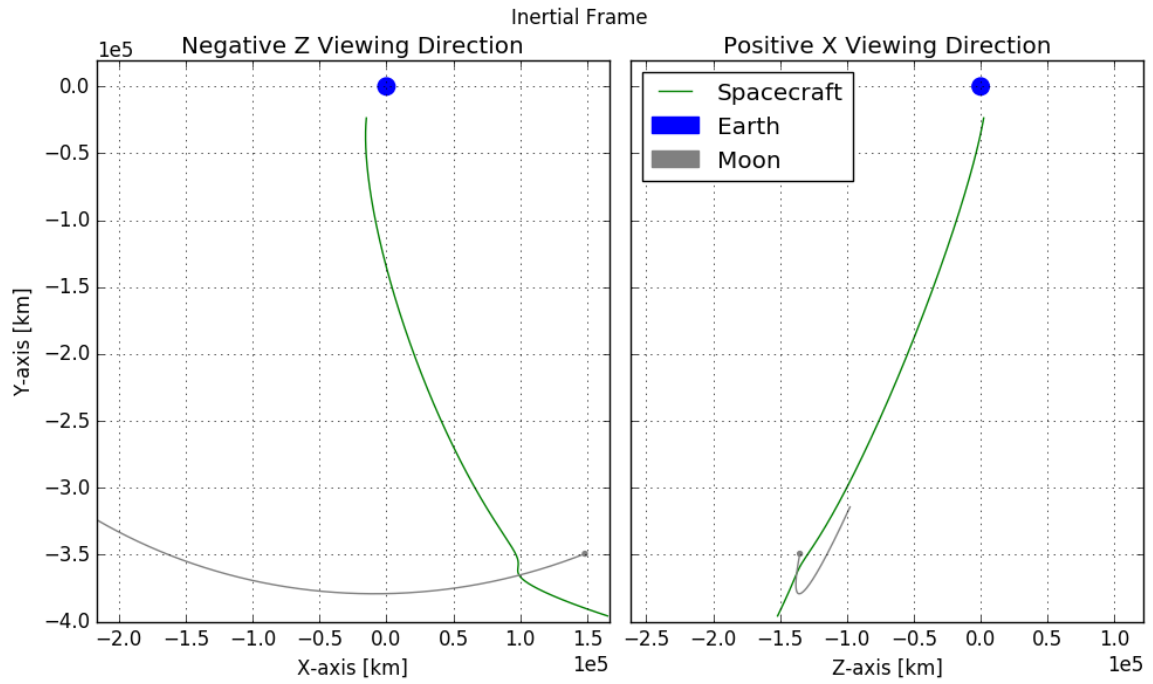
1. BALLISTIC TRAJECTORY

Figure 1. Ballistic trajectory viewed along the negative Z and positive X direction of the Earth-centered inertial frame.

2. PERILUNE 1

Figure 2. Perilune 1 trajectory with one instantaneous ΔV applied at perilune viewed along the negative Z and positive X direction of the Earth-centered inertial frame.

3. DISPOSAL 1 AND DISPOSAL 2

Scenarios in this section utilize a burn following disposal from the ICPS and at perilune as described in Section 3.3.

3.1. DISPOSAL 1

Figure 3. Disposal 1 trajectory viewed along the negative Z and positive X direction of the Earth-centered inertial frame.

3.2. DISPOSAL 2

Figure 4. Disposal 2 trajectory viewed along the negative Z and positive X direction of the Earth-centered inertial frame.

4. VAN ALLEN 1 AND VAN ALLEN 2
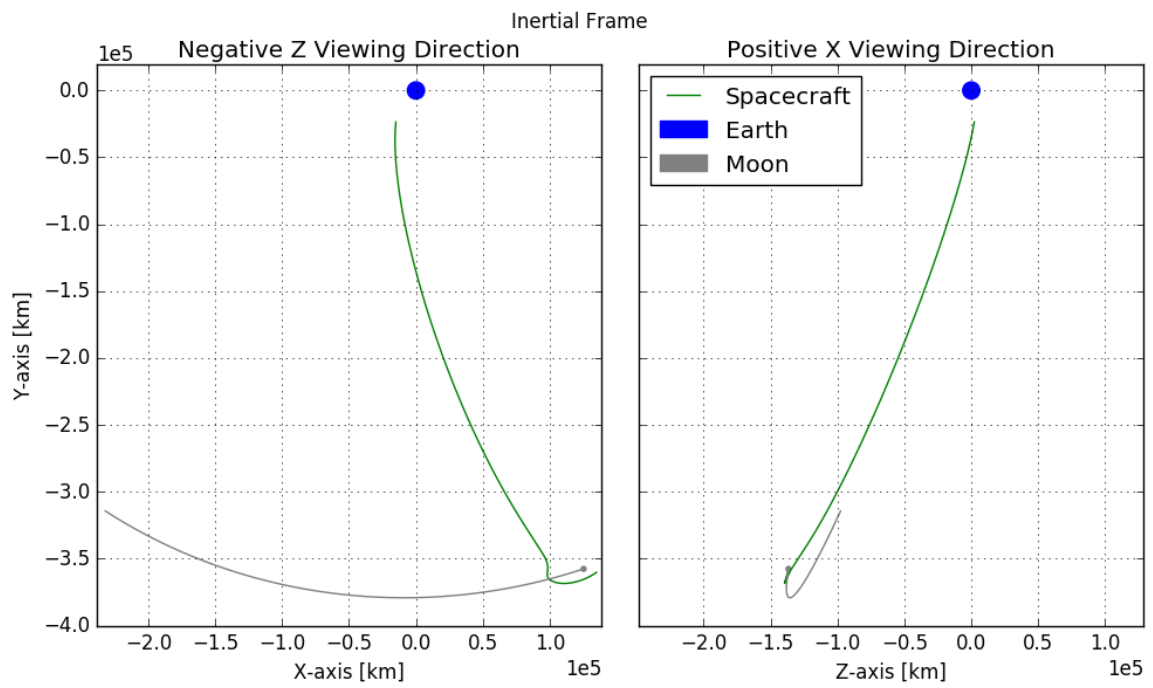
Scenarios in this section utilize a burn at the edge of the Van Allen radiation belt and at perilune as described in Section 3.3.
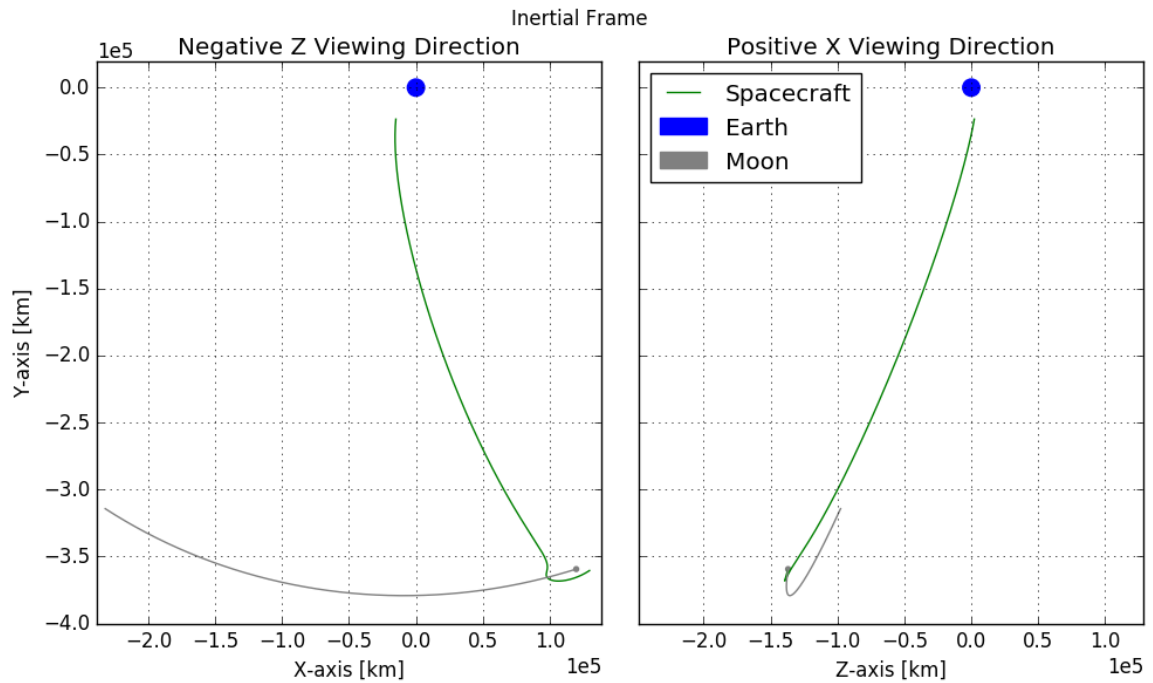
4.1. VAN ALLEN 1
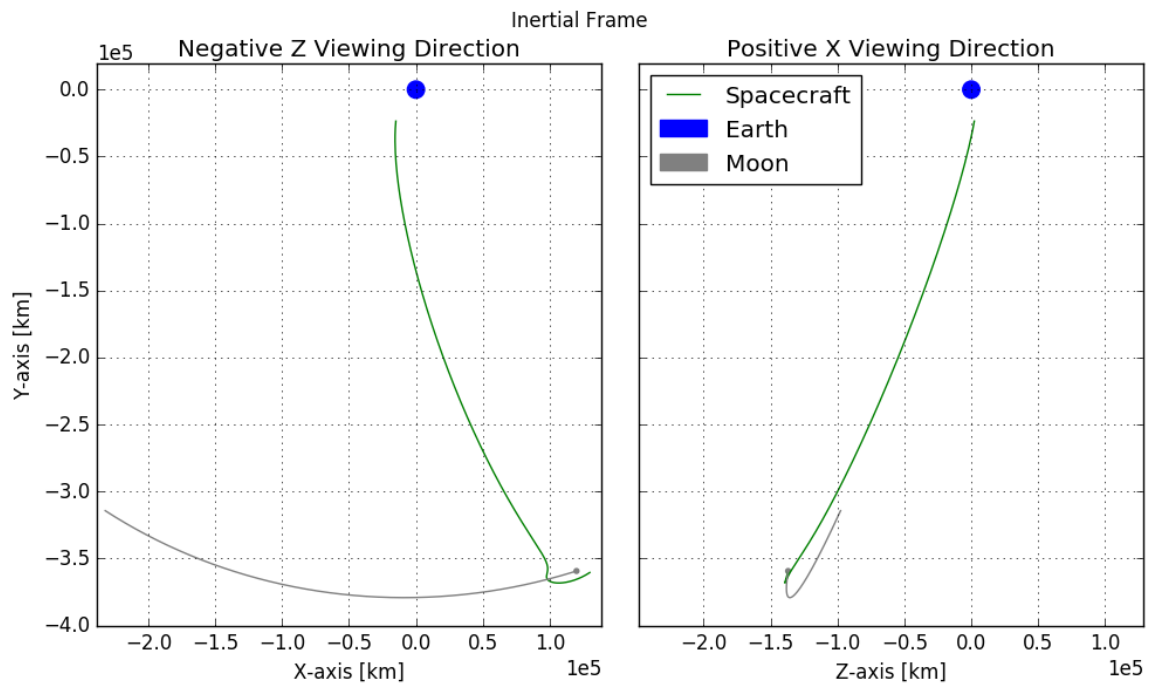
Figure 5. Van Allen 1 trajectory viewed along the negative Z and positive X direction of the Earth-centered inertial frame.

4.2. VAN ALLEN 2
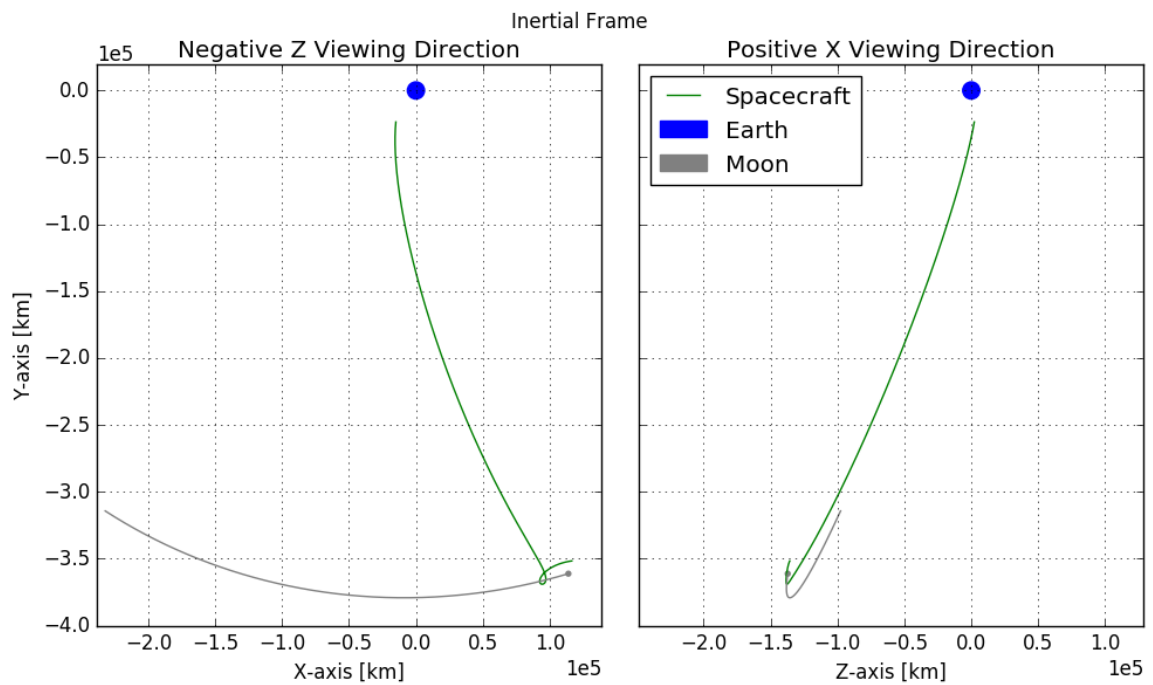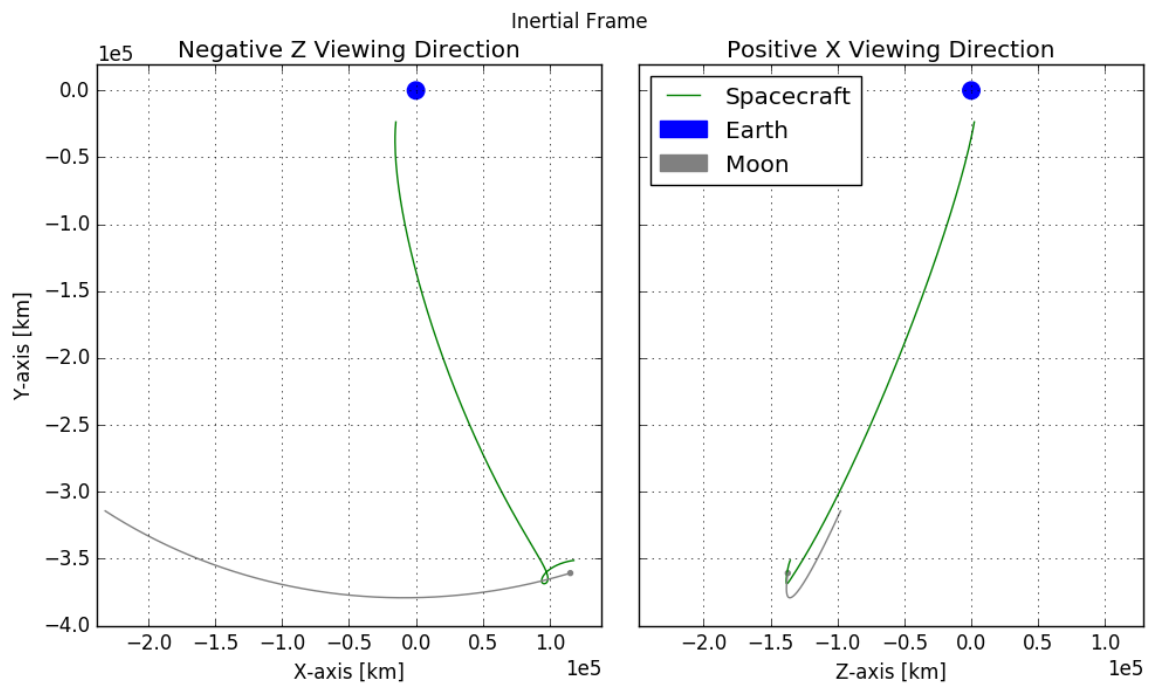

Figure 6. Van Allen 2 trajectory viewed along the negative Z and positive X direction of the Earth-centered inertial frame.

5. HIGH-FIDELITY MODEL

Plots in this section were generated using GMAT and are supplemental to those shown in Section 4.

5.1. BALLISTIC TRAJECTORY
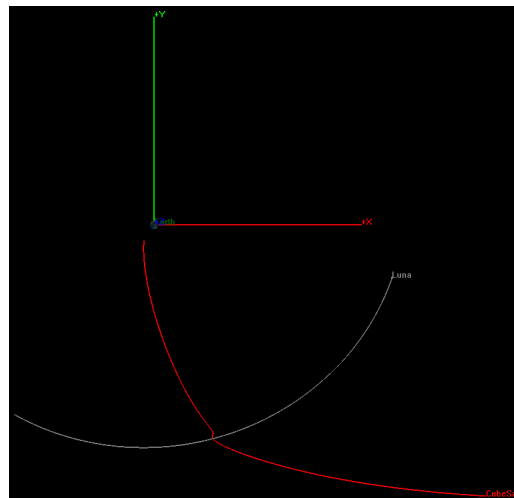
Figure 7. The ballistic trajectory simulated in GMAT and viewed along the X-Y plane of the Earth-centered inertial frame.
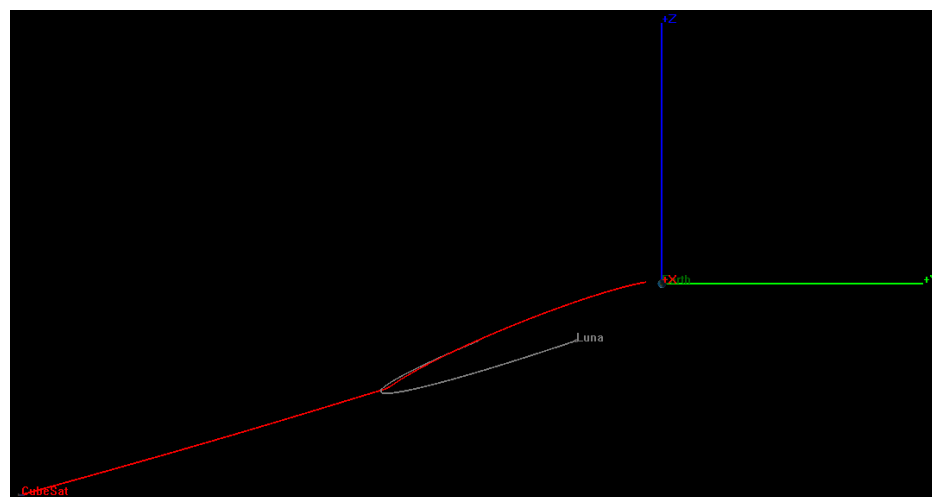
Figure 8. The ballistic trajectory simulated in GMAT and viewed along the Y-Z plane of the Earth-centered inertial frame.

5.2. IMPULSE AT PERILUNE (PERILUNE 1)
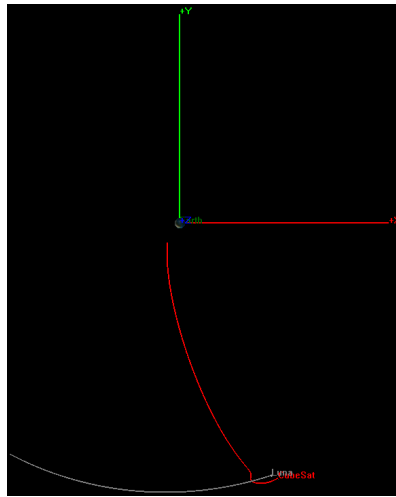
Figure 9. The Perilune 1 trajectory simulated in GMAT with one instantaneous ΔV applied at perilune, viewed along the negative Z direction of the X-Y plane of the Earth-centered inertial frame.
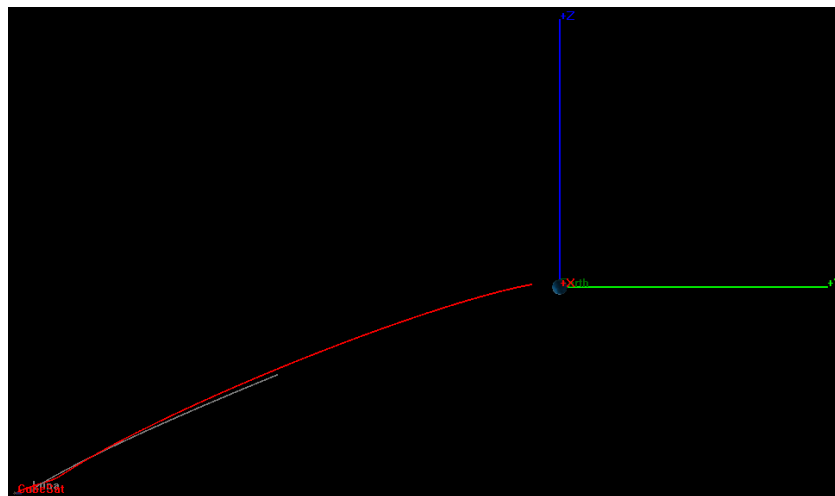
Figure 10. The Perilune 1 trajectory simulated in GMAT with one instantaneous ΔV applied at perilune, viewed along the negative X direction of the Y-Z plane of the Earth-centered inertial frame.

5.3. DISPOSAL 1 AND DISPOSAL 2

Scenarios in this section utilize a burn following disposal from the ICPS and at perilune as described in Section 3.3.

5.3.1. Disposal 1.

Figure 11. The Disposal 1 trajectory simulated in GMAT and viewed along the negative Z direction of the X-Y plane of the inertial frame.

Figure 12. The Disposal 1 trajectory simulated in GMAT and viewed along the negative X direction of the Y-Z plane of the inertial frame.

5.3.2. Disposal 2.

Figure 13. The Disposal 2 trajectory simulated in GMAT and viewed along the negative Z direction of the X-Y plane of the inertial frame.

Figure 14. The Disposal 2 trajectory simulated in GMAT and viewed along the negative X direction of the Y-Z plane of the inertial frame.

5.4. VAN ALLEN 1 AND VAN ALLEN 2

Scenarios in this section utilize a burn at the edge of the Van Allen radiation belt and at perilune as described in Section 3.3.

5.4.1. Van Allen 1.
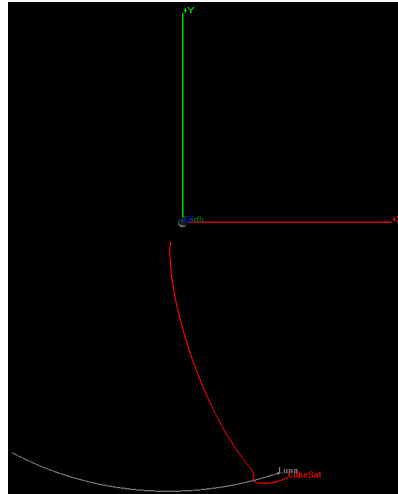
Figure 15. The Van Allen 1 trajectory simulated in GMAT and viewed along the negative Z direction of the X-Y plane of the inertial frame.
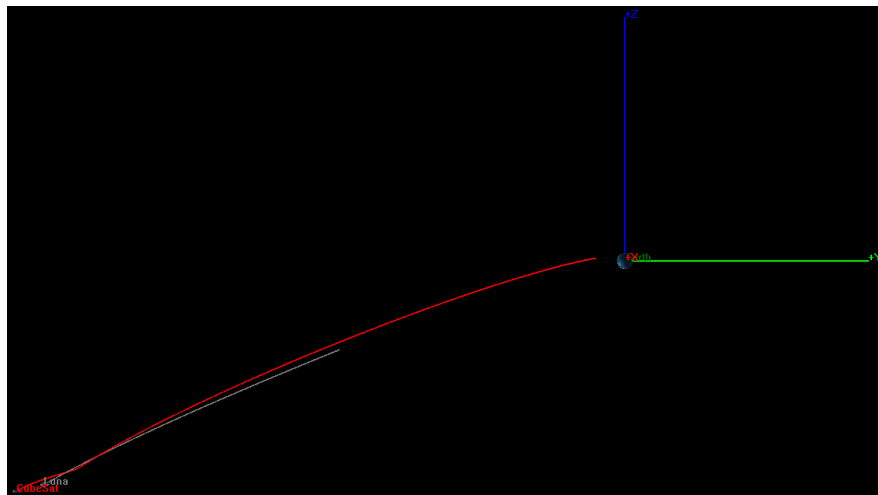
Figure 16. The Van Allen 1 trajectory simulated in GMAT and viewed along the negative X direction of the Y-Z plane of the inertial frame.

5.4.2. Van Allen 2.
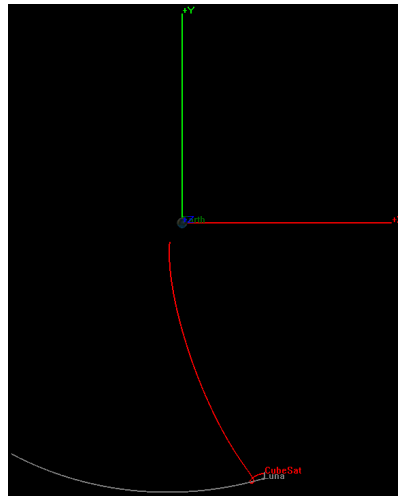
Figure 17. The Van Allen 2 trajectory simulated in GMAT and viewed along the negative Z direction of the X-Y plane of the inertial frame.
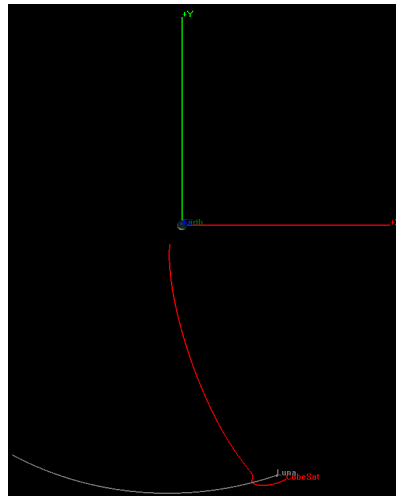

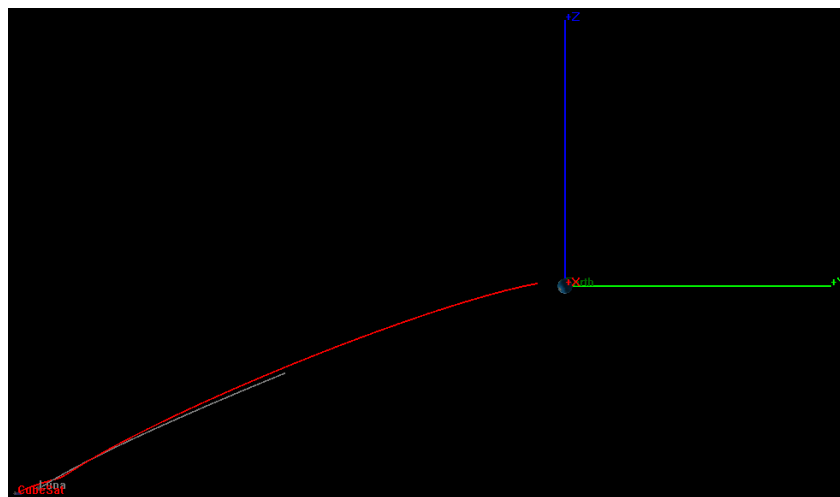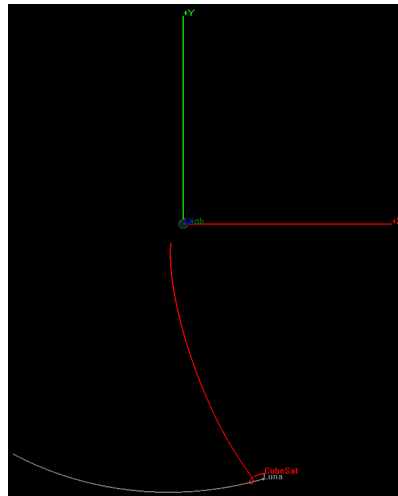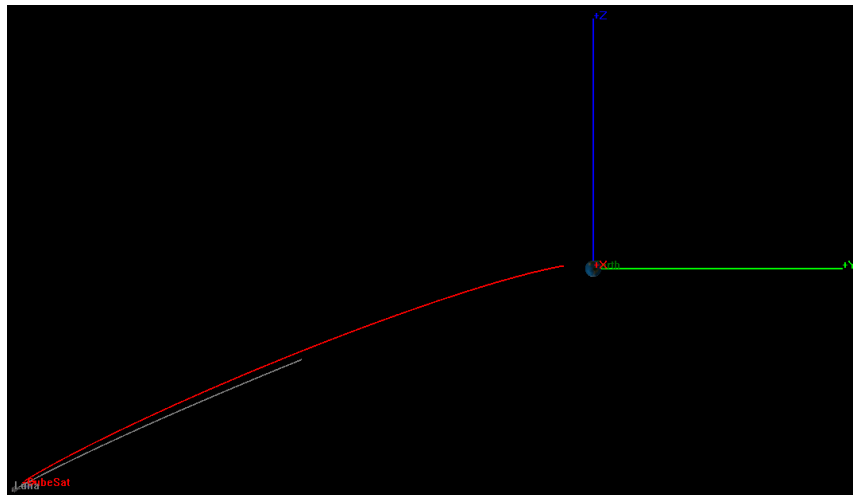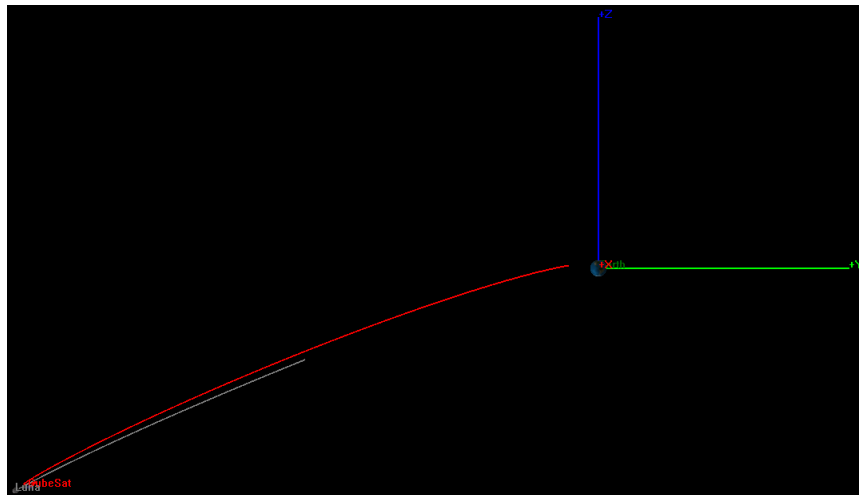Figure 18. The Van Allen 2 trajectory simulated in GMAT and viewed along the negative X direction of the Y-Z plane of the inertial frame.

APPENDIX B.

COMPUTATIONAL METHODS

The computational methods outlined below were implemented in Python for use in propagating the CR3BP and targeting parameters.

1. ORDINARY DIFFERENTIAL EQUATION SOLVER

Numerical integration is used through the form of an ordinary differential equation solver to calculate the state at some point in time. This is also referred to as propagation and applied to the CR3BP to compute the trajectory forward in time. LSODA stems from the Livermore Solver for Ordinary Differential Equations (LSODE) with the added capability by Linda Petzold to automatically switch methods for handling stiff and non-stiff systems [121, 124]. LSODA is in the FORTRAN ODEPACK, which is built into the SciPy package for use in Python 2.7 [121]. The relative and absolute tolerance were specified at 1×10^{-12} for all propagations as this is the minimum value possible without integration tolerance warnings from floating point limitations.

2. EXTREMUM FINDING

2.1. GOLDEN-SECTION SEARCH

Apoapsis and periapsis are the maximum and minimum distances to the central body origin. The golden-section search is capable of finding such points through an iterative process without the need of a derivative using the golden ratio (ϕ) shown below in equation 1 [122].

$$\phi = \frac{1 + \sqrt{5}}{2} \tag{1}$$

Let a and b bracket a maximum value with $f(a)$ and $f(b)$ being the output. The following equations show the calculation of c and d which are internal to a and b.

$$c = b - (b - a)/\phi \tag{2}$$

$$d = a + (b - a)/\phi \tag{3}$$

If $f(c)$ is less than $f(d)$, then b becomes d and the iteration starts over. If $f(d)$ is less than $f(c)$, then a becomes c and the iteration starts over. The process continues looping until a tolerance threshold is met and the final value is a maximum. For a minimum, the if statements are reversed or reverse the sign of the function output for a, b, c, and d [122]. The iterative process must meet a relative and absolute tolerance threshold of 1×10^{-12} as this is the maximum error allowed by the integrator.

2.2. NELDER-MEAD

The Nelder-Mead simplex method was published in 1965 by J. Nelder and R. Mead as a multidimensional minimization function and is now widely used [125, 126]. It applies a simplex of n + 1 points, where n is the number of dimensions, to adapt and contract around the minimum without the use of derivatives or tracking prior points, making it computationally small [125, 126, 127]. This direct search method is available in the SciPy package for Python 2.7 and was employed in this study to search for the minimum total ΔV by manipulating multiple burn angles [123, 128]. The convergence absolute tolerance was set to 1×10^{-12} for the input variables and the function output as this is the maximum error allowed by the integrator.

3. ROOT FINDING

The secant method, shown in equation 4, is an open root-finding algorithm that requires two initial guesses, x_{n-1} and x_{n-2}, to converge on a root of $f(x)$. Because this is an open method, the root is not required to be bracketed by the two initial values [122]. The

two values will produce x_n which will replace x_{n-1} in the next iteration while x_{n-1} replaces x_{n-2}. With each iteration the algorithm will converge on the root of f until a threshold is met.

$$x_n = \frac{x_{n-2}f(x_{n-1}) - x_{n-1}f(x_{n-2})}{f(x_{n-1}) - f(x_{n-2})} \tag{4}$$

In this research study, the iterative process is used to target a specified distance from the Earth or Moon and must meet a relative and absolute tolerance threshold of 1×10^{-12} km, as this is the maximum error allowed by the integrator. The secant method is utilized by subtracting a specified value from $f(x)$, the radial distance to the center of the Earth/Moon, which relocates the root so that $f(x_n)$ converges on the specified value. This enables the ability to target specific distances from the center of the Earth or Moon by subtracting these distances from the radial. Furthermore, by setting the independent variable as travel time or ΔV the secant method allows for the propagation of the spacecraft to end at a specified distance. For example, the outer edge of the Van Allen belt lies 64,307.984 km from the center of the Earth, and this distance was subtracted from the radial distance with respect to the Earth. Following multiple iterations with different travel times inputted for x, the state vector was identified at the point where the spacecraft reaches the outer edge of the Van Allen belt. A similar setup was applied where propagation ended at apolune or perilune with ΔV as the independent variable to target a specified distance at these locations.

REFERENCES

[1] Poghosyan, A. and Golkar, A., "CubeSat Evolution: Analyzing CubeSat Capabilities for Conducting Science," *Progress in Aerospace Sciences*, 2017, **88**, pp. 59–83.

[2] Mehrparvar, A., "CubeSat Design Specification Rev. 13," 2017.

[3] Nugent, R., Munakata, R., Chin, A., Coelho, R., and Puig-suari, D. J., "The Cube-Sat: The Picosatellite Standard for Research and Education," in *AIAA SPACE 2008 Conference & Exposition*, 2008 .

[4] Venturini, C. C., Abramowitz, L. R., Johansen, J. D., Gee, J. G., and Floyd, W. G., "CubeSat Development Programs-Working with the Community," in *AIAA SPACE 2009 Conference & Exposition*, 2009 .

[5] Amo, I. P., "CubeSat Concept Benefits," in *55th International Astronautical Congress 2004*, 2004 .

[6] NASA, "NASA Procedural Requirements for Limiting Orbital Debris and Evaluating the Meteoroid and Orbital Debris Environments," Technical Report 8715.6B, NASA, 2017.

[7] Humphries, Lt Col J., "Range Safety User Requirements Manual Volume 3 Launch Vehicles, Payloads, and Ground Support Systems Requirements," Technical Report 91-710, Air Force, 2004.

[8] Selva, D. and Krejci, D., "A Survey and Assessment of the Capabilities of CubeSats for Earth Observation," *Acta Astronautica*, 2012, **74**, pp. 50–68, doi: 10.1016/j.actaastro.2011.12.014.

[9] Paine, T. and Saing, M., "Ames Micro/Nanosatellites Cost Model," 2015.

[10] ESA, "CubeSats - Fly Your Satellite!" http://www.esa.int/Education/CubeSats_-_Fly_Your_Satellite/Fly_Your_Satellite!_programme, 2019, accessed 2018-01-14.

[11] Jackson, S., "About CubeSat Launch Initiative," https://www.nasa.gov/content/about-cubesat-launch-initiative, 2017, accessed 2018-01-14.

[12] Lan, W., Brown, J., Toorian, A., Coelbo, R., Brooks, L., Puig-Suari, J., and Twiggs, R., "CubeSat Development in Education and into Industry," in *Space 2006*, American Institute of Aeronautics and Astronautics, 2006 doi:10.2514/6.2006-7296.

[13] EnduroSat, "Onboard Computer (OBC) | CubeSat by EnduroSat," https://www.endurosat.com/products/cubesat-onboard-computer-obc/, 2016, accessed 2018-01-14.

[14] ISIS, "ISIS On Board Computer | ISIS - Innovative Solutions in Space," https://www.isispace.nl/product/on-board-computer/, 2016, accessed 2018-01-14.

[15] EnduroSat, "UHF Transceiver II CubeSat Communication | CubeSat by EnduroSat," https://www.endurosat.com/products/cubesat-transceiver-s-band-uhf/, 2017, accessed 2017-11-16.

[16] NanoAvionics, "CubeSat Communication Systems | NanoAvionics," http://n-avionics.com/cubesat-components/communication-systems/, 2017, accessed 2017-11-15.

[17] EnduroSat, "CubeSat Antennas," https://www.endurosat.com/products/\# cubesat-antennas, 2017, accessed 2017-11-16.

[18] EnduroSat, "CubeSat Communication," https://www.endurosat.com/products/\# communication-modules, 2017, accessed 2017-11-16.

[19] Sinclair, "Optical Communications," http://www.sinclairinterplanetary.com/ opticalcomms, 2017, accessed 2017-11-15.

[20] Clark, C. S. and Simon, E., "Evaluation of Lithium Polymer Technology for Small Satellite Applications," in *21st Annual AIAA/USU*, Conference on Small Satellites, 2007 .

[21] Blue Canyon Technologies, "Power Systems - Blue Canyon Tech," http://bluecanyontech.com/power-systems/, 2017, accessed 2017-11-15.

[22] Pumpkin, "GPS Receiver Module (GPSRM 1) Kit," http://www.pumpkinspace.com/ store/p58/GPS_Receiver_Module\%28GPSRM_1%29_Kit.html, 2017, accessed 2017-11-15.

[23] NanoAvionics, "CubeSat GPS Receiver | NanoAvionics," http://n-avionics. com/cubesat-components/navigation-systems/cubesat-gps-receiver/, 2017, accessed 2017-11-15.

[24] SkyFox Labs, "SkyFox Labs | Products - Navigation," http://www.skyfoxlabs.com/ products?category=3, 2017, accessed 2017-11-15.

[25] Toribio, S., "Galileo: Mission Planning," in *Space OPS 2004 Conference*, American Institute of Aeronautics and Astronautics, 2004 doi:10.2514/6.2004-282-130.

[26] Daly, P. and Misra, P. N., "GPS and Global Navigation Satellite System (GLONASS)," in *Global Positioning System: Theory and Applications, Volume II*, pp. 243–272, American Institute of Aeronautics and Astronautics, 1996, doi: 10.2514/5.9781600866395.0243.0272.

[27] Blue Canyon Technologies, "Star Trackers - Blue Canyon Tech," http://bluecanyontech.com/star-trackers/, 2017, accessed 2017-11-15.

[28] Sinclair, "Star Trackers," http://www.sinclairinterplanetary.com/startrackers, 2017, accessed 2017-11-15.

[29] Blue Canyon Technologies, "Attitude Control Systems - Blue Canyon Tech," http://bluecanyontech.com/attitude-control-systems/, 2017, accessed 2017-11-15.

[30] NanoAvionics, "Small Satellite & CubeSat Propulsion Systems | NanoAvionics," http://n-avionics.com/propulsion-systems/, 2017, accessed 2017-11-15.

[31] Aerojet Rocketdyne, "Modular Propulsion Systems," http://www.rocket.com/sites/default/files/documents/CubeSat%20Mod%20Prop-2sided.pdf, 2019, accessed 2019-05-12.

[32] Busek Co. Inc., "BGT-X5 Green Monopropellant Thruster," http://busek.com/index_htm_files/70008517E.pdf, 2018, accessed 2019-01-15.

[33] Busek Co. Inc., "BIT-3 RF Ion Thruster," http://busek.com/index_htm_files/70010819D.pdf, 2018, accessed 2019-01-15.

[34] VACCO, "Lunar Flashlight Propulsion System," https://www.cubesat-propulsion.com/lunar-flashlight-propulsion-system/, 2018, accessed 2019-01-15.

[35] Lemmer, K., "Propulsion for CubeSats," *Acta Astronautica*, 2017, **134**, p. 231, copyright - Copyright Elsevier BV May 2017; Last updated - 2017-11-14.

[36] VACCO, "JPL MarCO Micro CubeSat Propulsion System," https://www.cubesat-propulsion.com/jpl-marco-micro-propulsion-system/, 2018, accessed 2019-01-15.

[37] Technology Applications, Inc., "Thermal Straps | TAI," https://www.techapps.com/thermal-straps, 2016, accessed 2017-11-19.

[38] Thermotive, "Thermotive | High Conductance Thermal Straps for Cryocooler & Cryogenics," http://www.thermotive.com/thermalstraps.html, 2017, accessed 2017-11-19.

[39] Osaretin, I. A., Shields, M. W., Lorenzo, J. A. M., and Blackwell, W. J., "A Compact 118-GHz Radiometer Antenna for the Micro-Sized Microwave Atmospheric Satellite," *IEEE Antennas and Wireless Propagation Letters*, 2014, **13**, pp. 1533–1536, ISSN 1536-1225, doi:10.1109/LAWP.2014.2343155.

[40] Kramer, H. J., "IceCube - Satellite Missions - eoPortal Directory," https://directory.eoportal.org/web/eoportal/satellite-missions/i/icecube, 2017, accessed 2018-02-18.

[41] Kramer, H. J., "RAVAN - Satellite Missions - eoPortal Directory," https://directory.eoportal.org/web/eoportal/satellite-missions/r/ravan, 2017, accessed 2017-11-28.

[42] Cahoy, K., Marinan, A., Marlow, W., Cordeiro, T., Blackwell, W. J., Bishop, R., and Erickson, N., "Development of the Microwave Radiometer Technology Acceleration (MiRaTA) CubeSat for all-weather atmospheric sounding," in *2015 IEEE International Geoscience and Remote Sensing Symposium (IGARSS)*, IEEE, 2015 doi:10.1109/igarss.2015.7327032.

[43] Jackson, S., "Upcoming ElaNa CubeSat Launches," https://www.nasa.gov/content/upcoming-elana-cubesat-launches, 2017, accessed 2018-03-02.

[44] Kramer, H. J., "TEMPEST-D - Satellite Missions - eoPortal Directory," https://directory.eoportal.org/web/eoportal/satellite-missions/t/tempest-d, 2017, accessed 2018-02-18.

[45] Ranvier, S., Anciaux, M., Cardoen, P., Gamby, E., Bonnewijn, I. S., Keyser, J. D., Pieroux, D., and Lebreton, J. P., "Use of a Langmuir Probe Instrument on Board a Pico-Satellite," *IEEE Transactions on Plasma Science*, 2017, **45**(8), pp. 2007–2012, ISSN 0093-3813, doi:10.1109/TPS.2017.2700211.

[46] Osterman, D. P., Collins, S., Ferguson, J., Good, W., Kampe, T., Rohrschneider, R., and Warden, R., "CIRiS: Compact Infrared Radiometer in Space," in T. S. Pagano, editor, *CubeSats and NanoSats for Remote Sensing*, SPIE, 2016 doi:10.1117/12.2238999.

[47] Sarda, K., Grant, C., Eagleson, S., Kekez, D., and Zee, R., "Canadian Advanced Nanospace Experiment 2: On-orbit Experiences with a Three-kilogram Satellite," 2008.

[48] Rani, B. S., Gomathy, C., Sowmya, B., and Narmadha, R., "Attitude Determination and Control System of Sathyabamasat," in *Recent Advances in Space Technology Services and Climate Change 2010 (RSTS CC-2010)*, 2010 pp. 326–329, doi:10.1109/RSTSCC.2010.5712821.

[49] Praks, J., Kestila, A., Tikka, T., Nasila, A., Riwanto, B., Jovanovic, N., Niemela, P., Silva, N., Vainio, R., and Janhunen, P., "Aalto-1 Earth Observation nanosatellite mission status and in orbit experiments," in *2017 XXXIInd General Assembly and Scientific Symposium of the International Union of Radio Science (URSI GASS)*, IEEE, 2017 doi:10.23919/ursigass.2017.8105284.

[50] Pagano, T. S., "CubeSat infrared atmospheric sounder (CIRAS) NASA InVEST technology demonstration," in B. F. Andresen, G. F. Fulop, C. M. Hanson, J. L. Miller, and P. R. Norton, editors, *Infrared Technology and Applications XLIII*, SPIE, 2017 doi:10.1117/12.2266282.

[51] Pagano, T. S., Rider, D., Teixeira, J., Aumann, H., Rud, M., Pereira, J., Furlong, D., and Mamula, D., "The CubeSat Infrared Atmospheric Sounder (CIRAS), Pathfinder for the Earth Observing Nanosatellite-Infrared (EON-IR)," 2016.

[52] Carreno-Luengo, H., Ca, A., Perez-Ramos, I., Forte, G., Onrubia, R., and DÃŋez, R., "3Cat-2: A P(Y) and C/A GNSS-R Experimental Nano-satellite Mission," in *2013 IEEE International Geoscience and Remote Sensing Symposium - IGARSS*, ISSN 2153-6996, 2013 pp. 843–846, doi:10.1109/IGARSS.2013.6721290.

[53] Kramer, H. J., "Firefly - eoPortal Directory - Satellite Missions," https://directory. eoportal.org/web/eoportal/satellite-missions/f/firefly, 2017, accessed 2017-11-29.

[54] Neilsen, T. L., Martins, J. V., Fernandez Borda, R. A., Weston, C., Frazier, C., Cieslak, D., and Townsend, K., "The Hyper-Angular Rainbow Polarimeter (HARP) CubeSat Observatory and the Characterization of Cloud Properties," *AGU Fall Meeting Abstracts*, 2015, A43A-0237.

[55] Crowley, G., Fish, C. S., Bust, G. S., Swenson, C., Barjatya, A., and Larsen, M. F., "Dynamic Ionosphere Cubesat Experiment (DICE)," *AGU Fall Meeting Abstracts*, 2009, SM42A-06.

[56] Kramer, H. J., "CINEMA - eoPortal Directory - Satellite Missions," https:// directory.eoportal.org/web/eoportal/satellite-missions/c-missions/cinema, 2017, accessed 2018-01-10.

[57] Peral, E., Tanelli, S., Haddad, Z., Sy, O., Stephens, G., and Im, E., "Raincube: A Proposed Constellation of Precipitation Profiling Radars in CubeSat," in *2015 IEEE International Geoscience and Remote Sensing Symposium (IGARSS)*, ISSN 2153-6996, 2015 pp. 1261–1264, doi:10.1109/IGARSS.2015.7326003.

[58] Keesey, L., "Lunar IceCube to Take on Big Mission From Small Package," https://www.nasa.gov/feature/goddard/ lunar-icecube-to-take-on-big-mission-from-small-package, 2015.

[59] Harbaugh, J., "LunaH-Map: University-Built CubeSat to Map Water-Ice on the Moon," https://www.nasa.gov/feature/ lunah-map-university-built-cubesat-to-map-water-ice-on-the-moon, 2016.

[60] Cohen, B. A., Hayne, P. O., Paige, D. A., and Greenhagen, B. T., "Lunar Flashlight: Mapping Lunar Surface Volatiles Using a CubeSat," *Annual Meeting of the Lunar Exploration Analysis Group*, 2014.

[61] JPL, "JPL | Cubesat | Lunar Flashlight," https://www.jpl.nasa.gov/cubesat/missions/ lunar_flashlight.php, 2017, accessed 2018-01-09.

[62] McNutt, L., Johnson, L., Clardy, D., Castillo-Rogez, J., Frick, A., and Jones, L., "Near-Earth Asteroid Scout," *AIAA SPACE 2014 Conference and Exposition*, 2014.

[63] JPL, "JPL | Cubesat | INSPIRE," https://www.jpl.nasa.gov/cubesat/missions/inspire. php, 2017, accessed 2018-01-09.

[64] Greicius, T., "Farewell to Mars," https://blogs.nasa.gov/insight/2018/11/26/ farewell-to-mars/, 2018, accessed 2019-04-15.

[65] Frazier, S., "Heliophysics CubeSat to Launch on NASA's SLS," https://www.nasa.gov/feature/goddard/2016/heliophysics-cubesat-to-launch-on-nasa-s-sls, 2016.

[66] Brown, K. Z., Rose, T. G., Malphrus, B. K., Kruth, J. A., Thomas, E. T., Combs, M. S., McNeil, R., Kroll, R. T., Cahall, B. J., Burba, T. T., Molton, B. L., Powell, M. M., Fitzpatrick, J. F., Graves, D. C., Jernigan, J. G., Simms, L., Doty, J. P., Wampler-Doty, M., Anderson, S., Cominsky, L. R., Prasad, K. S., Gaalema, S. D., and Sun, S., "The Cosmic X-Ray Background NanoSat (CXBN): Measuring the Cosmic X-Ray Backgorund Using the CubeSat Form Factor," *26th Annual AiAA/USU Conference on Small Satellites*, 2012.

[67] Knapp, M. and Seager, S., "ASTERIA: A CubeSat for Exoplanet Transit and Stellar Photometry," in *AAS/Division for Extreme Solar Systems Abstracts*, Volume 3 of *AAS/Division for Extreme Solar Systems Abstracts*, 2015 p. 106.08.

[68] JPL, "JPL | CubeSat | ASTERIA," https://www.jpl.nasa.gov/cubesat/missions/asteria.php, 2017, accessed 2018-01-10.

[69] Lovis, C. and Fischer, D. A., *Radial Velocity*, Yale University Press, 2010.

[70] Kramer, H. J., "PicSat - eoPortal Directory - Satellite Missions," https://directory.eoportal.org/web/eoportal/satellite-missions/p/picsat, 2017, accessed 2018-01-10.

[71] VerticalNews, "NASA/Goddard Space Flight Center; NASA's New Mini Satellite Will Study Milky Way's Halo," 2018, name - University of Iowa; Goddard Space Flight Center; International Space Station; Jet Propulsion Laboratory; Chandra X-ray Observatory; National Aeronautics & Space Administration–NASA; Johns Hopkins University; Copyright - Copyright 2018, NewsRx LLC; Last updated - 2018-08-13.

[72] Kaaret, P., "HaloSat - A CubeSat to Study the Hot Galactic Halo," in *AAS/High Energy Astrophysics Division*, Volume 15 of *AAS/High Energy Astrophysics Division*, 2016 p. 203.05.

[73] Space & Missile Defense Report, "Tiny Satellite To Probe Drug Effectiveness In Space," *Space & Missile Defense Report*, 2009, **32**(18), name - National Aeronautics & Space Administration; Copyright - (Copyright (c) 2009 Access Intelligence, LLC. All rights reserved.; Last updated - 2010-06-06.

[74] Hoover, R., "NASA Nanosatellite Studies Life in Space, Demonstrates Technology," Technical report, Federal Information & News Dispatch, Inc, 2010, name - NASA Ames Research Center; Copyright - Copyright (c) 2010 Federal Information & News Dispatch, Inc; Last updated - 2012-07-24.

[75] Kramer, H. J., "SporeSat - eoPortal Directory - Satellite Missions," https://directory.eoportal.org/web/eoportal/satellite-missions/s/sporesat, 2017, accessed 2018-01-11.

[76] Nehrenz, M. and Sorgenfrei, M., "On the Development of Spacecraft Operating Modes for a Deep Space CubeSat," *AIAA SPACE 2015 Conference and Exposition*, 2015.

[77] Colwell, J., Brisset, J., Dove, A., Blum, J., and Maukonen, D., "Q-PACE: A Long-Duration Microgravity Experiment on Planetesimal Formation," in *7th Interplanetary CubeSat Workshop*, 2018 .

[78] Nallapu, R., Shah, S., Asphaug, E., and Thangavelautham, J., "Attitude Control of the Asteroid Origins Satellite 1 (AOSAT 1)," 2017.

[79] Mahoney, E., "Past ElaNa CubeSat Launches," https://www.nasa.gov/content/past-elana-cubesat-launches, 2017, accessed 2018-03-02.

[80] Orbital ATK, "Mission Update: Minotaur C SkySat Launch," https://www.orbitalatk.com/news-room/feature-stories/MinotaurC_SkySat_Mission-Page/default.aspx?prid=283, 2017, accessed 2018-03-04.

[81] Schoneman, S., Amorosi, L., Laidley, M., Wilder, K., and Hunley, B., "Minotaur-Family Launch Vehicles Responsive Launch Demonstration for the TacSat-2 Mission," in *AIAA SPACE 2007 Conference & Exposition*, American Institute of Aeronautics and Astronautics, 2007 doi:10.2514/6.2007-6145.

[82] Thorpe, D. G. and Henderson, E. M., "Proposed Lunar Mission to Commemorate Apollo 11 Moon Landing," in *52nd AIAA/SAE/ASEE Joint Propulsion Conference*, American Institute of Aeronautics and Astronautics, 2016 doi:10.2514/6.2016-4515.

[83] Rocket Lab, "Rocket Lab | Electron - satellite launch vehicle | Rocket Lab," https://www.rocketlabusa.com/electron/, 2018, accessed 2018-03-01.

[84] Courtland, R., "Finish Line Looms for Google Lunar Xprize [News]," *IEEE Spectrum*, 2017, **54**(3), pp. 7–9, ISSN 0018-9235, doi:10.1109/MSPEC.2017.7864740.

[85] Skrobot, G., "Developing New Tools for the ELaNa," https://ntrs.nasa.gov/archive/nasa/casi.ntrs.nasa.gov/20160010319.pdf, 2016.

[86] Wagner, S., Pitz, A., Zimmerman, D., and Wie, B., "Interplanetary Ballistic Missile (IPBM) System Architecture Design for Near-Earth Object Threat Mitigation," *IAC-09 D*, 2009, **1**.

[87] Kinnersley, M. and Viertel, Y., "ROCKOT - A Light Class Launch System for Reliable Access to LEO," in *AIAA Space 2001 Conference and Exposition*, American Institute of Aeronautics and Astronautics, 2001 doi:10.2514/6.2001-4698.

[88] Drobakhin, O. I., Konyukhov, S. N., Us, S. I., Andreyev, V. A., Mikhailov, V. S., and Solovey, V. A., "Layout Selection of Upper Space Tugs For Solution of Dnepr SRC High-Performance Problems," in *55th International Astronautical Congress of the International Astronautical Federation, the International Academy of Astronautics, and the International Institute of Space Law*, American Institute of Aeronautics and Astronautics, 2004 doi:10.2514/6.iac-04-v.3.02.

[89] Singer, J. A., Cook, J. R., and Singer, C. E., "NASA Space Launch System Operations Strategy," in *Space Operations: Experience, Mission Systems, and Advanced Concepts*, pp. 153–168, American Institute of Aeronautics and Astronautics, Inc., 2013, doi:10.2514/5.9781624102080.0153.0168.

[90] Hefner, W. K., Matisak, B. P., McElyea, R. M., Kunz, J. C., Weber, P. J., Cummings, N. H., and Parsons, J. W., "NASA Space Launch System Operations Outlook," *SpaceOps 2014 Conference*, 2014.

[91] Cichan, T., Norris, S. D., and Marshall, P. F., "Orion: EFT-1 Flight Test Results and EM-1/2 Status," *AIAA SPACE 2015 Conference and Exposition*, 2015.

[92] NASA, "Forward to the Moon: NASA's Strategic Plan for Human Exploration," https://www.nasa.gov/sites/default/files/atoms/files/america_to_the_moon_2024_artemis_20190523.pdf, 2019, accessed 2019-09-26.

[93] Donahue, B. B., Burks, D., Cooper, D., and Post, K., "Scientific and Human Exploration Opportunities Enabled by the Space Launch System," *AIAA SPACE 2015 Conference and Exposition*, 2015.

[94] Norris, S. D. and Marshall, P. F., "Orion Program Status," *AIAA SPACE 2013 Conference and Exposition*, 2013.

[95] Mahoney, E., "NASA Selects Lockheed Martin's SkyFire CubeSat for EM-1 Secondary Payload," https://www.nasa.gov/feature/nasa-selects-lockheed-martin-s-skyfire-cubesat-for-em-1-secondary-payload, 2016.

[96] Parker, J. S. and Anderson, R. L., *Low-Energy Lunar Trajectory Design*, JPL Deep-Space Communications and Navigation Series, John Wiley & Sons, Inc., 2014.

[97] Siddiqi, A. A., *Deep Space Chronicle: A Chronology of Deep Space and Planetary Probes, 1958-2000*, Monographs in Aerospace History, National Aeronautics and Space Administration, Office of External Relations, NASA History Office, 2002.

[98] Williams, D. and Friedlander, J., "Earth's Moon - Luna 3," https://nssdc.gsfc.nasa.gov//imgcat//hires//lu3_1.gif, 2016.

[99] Williams, D. R., "Zond 5," https://nssdc.gsfc.nasa.gov/nmc/spacecraftDisplay.do?id=1968-076A, 2017, accessed 2017-03-27.

[100] Brooks, C. G., Grimwood, J. M., and Jr., L. S. S., *Chariots for Apollo: A History of Manned Lunar Spacecraft*, NASA History Series, Washington, DC : Scientific and Technical Information Branch, National Aeronautics and Space Administration, 1979, ISBN 9780486467566, accessed 2017-04-03.

[101] Orloff, R. W., *Apollo by the Numbers: A Statistical Reference*, The NASA History Series, Washington, DC : Scientific and Technical Information Branch, National Aeronautics and Space Administration, 2000, ISBN 9780486467566, accessed 2017-04-04.

[102] Kauderer, A., "Apollo Imagery," https://spaceflight.nasa.gov/gallery/images/apollo/apollo8/html/as08-14-2383.html, 2012, accessed 2017-04-05.

[103] Williams, D. R., "Hiten," https://nssdc.gsfc.nasa.gov/nmc/spacecraftDisplay.do?id=1990-007A, 2017, accessed 2017-03-26.

[104] Cosgrove, D., Frey, S., Marchese, J., Owens, B., and Bester, M., "ARTEMIS Operations from Earth-Moon Libration Orbits to Stable Lunar Orbits," *SpaceOps 2012 Conference*, 2012.

[105] Cosgrove, D., Frey, S., Marchese, J., Owens, B., Gandhi, S., and Bester, M., "Navigating THEMIS to the ARTEMIS Low-Energy Lunar Transfer Trajectory," *SpaceOps 2010 Coference*, 2010.

[106] Koon, W. S., Lo, M. W., Marsden, J. E., and Ross, S. D., "Shoot the Moon," 2000.

[107] Gestal, D., Camino, O., Alonso, M., Milligan, D., Blake, R., de Bruin, J., Ricken, S., and Voss, P. P., "SMART-1 Operations," in *56th International Astronautical Congress of the International Astronautical Federation, the International Academy of Astronautics, and the International Institute of Space Law*, International Astronautical Congress (IAF), American Institute of Aeronautics and Astronautics, 2005, doi:10.2514/6.IAC-05-B5.3.B5.5.10.

[108] Fox, K. C., "NASA's Van Allen Probes Spot an Impenetrable Barrier in Space," https://www.nasa.gov/content/goddard/van-allen-probes-spot-impenetrable-barrier-in-space, 2017, accessed 2018-07-26.

[109] Vallado, D. A., *Fundamentals of Astrodynamics and Applications*, Springer-Verlag New York, third edition, 2007.

[110] Wiesel, W. E., *Spaceflight Dynamics*, Aphelion Press, third edition, 2010.

[111] The GMAT Development Team, *General Mission Analysis Tool (GMAT) Mathematical Specifications DRAFT*, NASA Goddard Space Flight Center, draft for release r2017a edition, 2017.

[112] a.i. solutions, "FreeFlyer Space Software Capabilities Summary," https://ai-solutions.com/wp-content/uploads/2017/12/12132017-FreeFlyer-Space-Software-Capabilities-Summary.pdf, 2017, accessed 2018-01-16.

[113] AGI, "Astrogator Product Specsheet," https://p.widencdn.net/1lnihh/Astrogator-Product-Specsheet, 2017, accessed 2018-01-16.

[114] Sincarsin, G. B. and Hughes, P. C., "Torque from Solar Radiation Pressure Gradient During Eclipse," *Journal of Guidance, Control, and Dynamics*, 1983, **6**(6), pp. 511–517, doi:10.2514/3.8532.

[115] AGI, "SatPro Product Specsheet," https://p.widencdn.net/7cxuoa/SatPro--Product-Specsheet, 2017, accessed 2018-01-16.

[116] NASA Centennial Challenges in Collaboration with Ames Research Center, "Operations and rules," https://www.nasa.gov/sites/default/files/atoms/files/ccp_cq_opsrul_001c2.pdf, 2015.

[117] Williams, D. R., "Moon Fact Sheet," https://nssdc.gsfc.nasa.gov/planetary/factsheet/moonfact.html, 2017, accessed 2018-04-15.

[118] NASA, "ICPS Disposal State," https://www.nasa.gov/sites/default/files/sls_secondary_payload_trajectory_20141017rev1.docx, 2014.

[119] Chamberlin, A., "HORIZONS Web-Interface," https://ssd.jpl.nasa.gov/horizons.cgi, 2016, accessed 2016-01-25.

[120] NASA, "GMAT User Guide R2016a," http://gmat.sourceforge.net/doc/R2016a/help-letter.pdf, 2016, accessed 2019-03-01.

[121] Hindmarsh, A., "ODEPACK, A Systematized Collection of ODE Solvers," in *Scientific Computing*, Volume 1 of *IMACS Transactions on Scientific Computation*, pp. 55–64, 1983.

[122] Chapra, S. C. and Canale, R. P., *Numerical Methods for Engineers*, McGraw-Hill, sixth edition, 2010.

[123] Dennis, J. and Woods, D. J., "Optimization on Microcomputers: The Nelder-Mead Simplex Algorithm," *New Computing Environments: Microcomputers in Large-scale Computing*, 1987, **11**, pp. 6–122.

[124] Petzold, L., "Automatic Selection of Methods for Solving Stiff and Nonstiff Systems of Ordinary Differential Equations," *SIAM Journal on Scientific and Statistical Computing*, 1983, **4**(1).

[125] Nelder, J. A. and Mead, R., "A Simplex Method for Function Minimization," *The Computer Journal*, 1965, **7**(4), pp. 308–313, doi:10.1093/comjnl/7.4.308.

[126] Lagarias, J., Reeds, J., Wright, M., and Wright, P., "Convergence Properties of the Nelder–Mead Simplex Method in Low Dimensions," *SIAM Journal on Optimization*, 1998, **9**(1), pp. 112–147, doi:10.1137/S1052623496303470.

[127] Olsson, D. M. and Nelson, L. S., "The Nelder-Mead Simplex Procedure for Function Minimization," *Technometrics*, 1975, **17**(1), pp. 45–51, doi:10.1080/00401706.1975.10489269.

[128] SciPy, "scipy.optimize.fmin," https://docs.scipy.org/doc/scipy/reference/generated/scipy.optimize.fmin.html, 2017, accessed 2017-09-04.

VITA

Garrett Levi McMillan was born in Portsmouth, Virginia and spent most of his childhood moving around and in various schools until settling in Cape Girardeau, MO where he graduated from Cape Central High School in May 2008. Garrett then attended a two-year engineering transfer program at Southeast Missouri State University before transitioning to Missouri University of Science and Technology to pursue a degree in Aerospace Engineering. He became an active member of the Missouri University of Science and Technology Satellite Research Team (M-SAT) and became Lead of the Orbit subsystem for a nanosatellite project. Garrett earned a Bachelor of Science in Aerospace Engineering in May 2013. Following graduation, he pursued a Master of Science in Aerospace Engineering at Missouri University of Science and Technology while simultaneously participating in out-of-state co-ops and internships. While taking courses on campus, he remained an active member of M-SAT and became Lead of the Trajectory subsystem for a Lunar CubeSat project and went on further to become Chief Engineer. Additionally, Garrett was a research assistant for the AREUS lab in the Mechanical and Aerospace Department. Upon completion of his on-site coursework, Garrett accepted full-time employment for an aerospace company in Hawthorne, California. In December 2019, Garrett received a Master of Science in Aerospace Engineering from Missouri University of Science and Technology.